NTNU

Norwegian University of
Science and Technology

Development of Hydrophobic Surfaces for Anti-Icing Applications

Vegard Hornnes

Nanotechnology

Submission date: June 2017

Supervisor: Hilde Lea Lein, IMA

Co-supervisor: Sidsel Hanetho, SINTEF
Christian Simon, SINTEF
Per Martin Stenstad, SINTEF

Norwegian University of Science and Technology
Department of Materials Science and Engineering

Abstract

Ice accumulation on outdoor infrastructure is a major problem for many industries. Several strategies are commonly employed to remove ice, but they are often expensive or have negative environmental consequences. An alternative strategy is to utilize anti-icing surfaces, which can prevent ice formation or make it easier to remove. A surface that has been investigated for its anti-icing properties are hydrophobic surfaces. These surfaces are extremely water-repellent, and they have also been shown to suppress icing and lower ice adhesion.

In this work, hydrophobic surfaces have been created on aluminium by combining a hierarchical roughness on the micro- and nanoscale with a low surface energy coating. Aluminium has been sandblasted with coarse and fine sand, resulting in two different microstructures. SiO_2 nanoparticles were synthesised and deposited through spray coating in different amounts, and were found to be 186 ± 12 nm in diameter. A low surface energy sol-gel coating based on the fluorosilane precursor 1H,1H,2H,2H-Perfluorooctyltriethoxysilane was synthesised and deposited in one or several layers via spray coating. The micro- and nanostructure that resulted from the experimental parameters were optimized. The most hydrophobic substrate was coarsely sandblasted, had SiO_2 nanoparticles and a single layer of fluorosilane coating. It demonstrated a contact angle of $165.7 \pm 1.3°$ and a contact angle hysteresis of $22.8 \pm 1.6°$.

The anti-icing properties of the hydrophobic surfaces have been investigated by measuring the temperature that water froze on the surfaces, the delay before water froze at $-10\,°C$ and the effect of several icing/deicing cycles. The freezing temperature was lowered significantly by the coating, but it was not affected by the microstructure. The lowest freezing temperature was $-13.1 \pm 1.1\,°C$ on a substrate with reduced nanoparticle deposition. The most hydrophobic substrate registered the longest freezing delay at 43 minutes. But other, less hydrophobic substrates also showed long freezing delays. Thus, no correlation between hydrophobicity and anti-icing properties was found. In addition, the humidity was found to have a major influence on the hydrophobicity and anti-icing properties, because of condensation and frost formation.

Sammendrag

Ising på installasjoner og infrastruktur er et betydelig problem for mange industrier. Flere ulike strategier brukes for å fjerne is, men de er ofte dyre eller de kan ha negative miljøkonsekvenser. En alternativ strategi er å bruke antiisende overflater, som kan forhindre ising eller gjøre den lettere å fjerne. En type overflate som har blitt undersøkt for dette bruksområdet er hydrofobe overflater. Disse overflatene er særdeles vannavstøtende, og de har også demonstrert evnen til å kunne forhindre ising og redusere isadhesjon.

I denne oppgaven har hydrofobiske overflater blitt dannet på aluminium ved å kombinere en hierarkisk ruhet på mikro- og nanoskala med et belegg med lav overflateenergi. Aluminium har blitt sandblåst med ru og fin sand, som resulterte i to ulike mikrostrukturer. SiO_2 nanopartikler ble dannet og deponert via spray coating i ulike mengder. Partiklene ble funnet å være 186 ± 12 nm i diameter. Et sol-gel belegg med lav overflateenergi basert på fluorsilanet 1H,1H,2H,2H-Perfluorooctyltriethoxysilane ble dannet og deponert i ett eller flere lag via spray coating. Mikro- og nanostrukturen som resulterte fra de eksperimentelle parametrene har blitt optimalisert. Det mest hydrofobiske substratet var sandblåst med ru sand, den hadde SiO_2 nanopartikler og et enkelt lag med fluorsilanbelegg. Den hadde en kontaktvinkel på $165.7 \pm 1.3°$ og en kontaktvinkelhysterese på $22.8 \pm 1.6°$.

Antiisingsegenskapene til de hydrofobiske overflatene har blitt undersøkt ved å måle frysetemperaturen til vann på overflatene, hvor lenge frysing ble forsinket ved $-10\,°C$ og effekten av flere ising/deising sykluser. Frysetemperaturen ble betraktelig nedsatt av belegget, men ble ikke påvirket av mikrostrukturen. Den laveste frysetemperaturen var $-13.1 \pm 1.1\,°C$ på et substrat med redusert konsentrasjon av nanopartikler. Det mest hydrofobiske substratet forsinket ising lengst med 43 minutter. Men andre, mindre hydrofobiske substrater forsinket også ising i en betydelig tid. Dermed ble det ikke funnet noen sammenheng mellom hydrofobisitet og antiisende egenskaper. I tillegg ble det funnet at fuktighet hadde en stor påvirkning på de hydrofobiske og antiisende egenskapene på grunn av kondens og dannelsen av frost.

Preface

This master's thesis was started in January 2016. Due to several delays caused by extended illness, it was finally completed in June 2017. The main experimental work was performed between December 2016 and June 2017. This thesis is the final part of my 5-year Master's degree program in Nanotechnology, with the specialization Nanotechnology for materials, energy and the environment at the Norwegian University of Science and Technology (NTNU).

The work was performed at the Department of Materials Science and Engineering, in the Inorganic Materials and Ceramics Research Group. Associate Professor Hilde Lea Lein has been my main supervisor, while Sidsel Meli Hanetho, Christian R. Simon and Per M. Stenstad, all at SINTEF, have been co-supervisors. This thesis is a continuation of the work performed by Hanna Vassmyr[1] in 2016, as well as by Raymond Luneng[2] and Ole-Bjørn Ellingsen Moe[3] in 2015. Harald Larssæter has also been working on the anti-icing project at the department. He has focused on characterizing the anti-icing and mechanical properties of commercial coatings. All the experimental work in this thesis was performed by the author.

Trondheim, 30.06.2017

Vegard Hornnes

Acknowledgement

The work performed during this thesis has been challenging, yet interesting. It would not have been completed were it not for the support from several people.

Firstly, I would like to thank my supervisor, Associate Professor Hilde Lea Lein. Your endless patience and support have been invaluable, and your enthusiasm for the project has been inspiring. Secondly, I would like to thank my co-supervisor Sidsel Meli Hanetho, for all your support, feedback and encouragement. Thank you to my other co-supervisors, Christian R. Simon and Per M. Stenstad, for your valuable input. I would also like to thank Hanna Vassmyr and Harald Larssæter, who have also been working on the anti-icing project. I am grateful for all our discussions and cooperation.

My gratitude also goes out to everyone at the Department who gave me training, offered feedback and answered my questions. The Research Council of Norway is acknowledged for the support to NTNU NanoLab through the Norwegian Micro- and Nano-Fabrication Facility, NorFab (197411/V30).

Lastly, I would like to thank my friends and family for their unwavering support.

Contents

List of Figures

List of Tables

List of Abbreviations

CA . . . . . Contact Angle

CAH . . . . . Contact Angle Hysteresis

DI Water . . . . De-ionized Water

TEOS . . . . . Tetraethyl orthosilicate

SEM . . . . . Scanning Electron Microscope

SE . . . . . Secondary Electron

BSE . . . . . Back-Scattered Electron

Chapter 1

Introduction

1.1 Motivation

Ice accumulation on outdoor infrastructure is a major problem for many industries that operate in cold regions. Overhead transmission lines, wind turbines, aircraft and offshore installations are all affected by icing.[4][5]. For overhead transmission lines, the extra weight added by ice growth lead to more frequent breakdowns and power outages . Lives can be endangered and economic losses can occur as a result[6][7][8]. Icing on wind turbines can lead to efficiency losses as the ice changes the aerodynamic properties of the turbine blades[9][10]. On aircraft, icing has led to numerous delays and several crashes[11][12]. Examples of icing on infrastructure is shown in figure 1.1.

Several strategies are commonly employed to deal with ice accumulation. They can typically be divided into two categories: deicing, or anti-icing. Deicing techniques are based on removing ice that has already formed through a variety of methods. For overhead transmission lines and wind turbines, ice is commonly removed through thermal or mechanical methods[15][16][17]. However, these methods demand either large amounts of energy or manpower. Icing on aircraft is typically removed through the use of salt or glycols, which represent significant costs and leads to groundwater contamination[12][18].

Clearly, there are several major disadvantages to the most commonly used deicing techniques. Another approach to the problem is to use anti-icing methods, which seeks to prevent ice from forming in the first place. Both active and passive anti-icing methods exist, with the central difference that active methods require some sort of energy input[16]. Passive methods on the other hand prevent icing without any external input. One such method is to modify the surface on which icing occurs.

There has been widespread research in the past ten years on what surface treatments can prevent icing[12]. One type of surface that has been investigated are

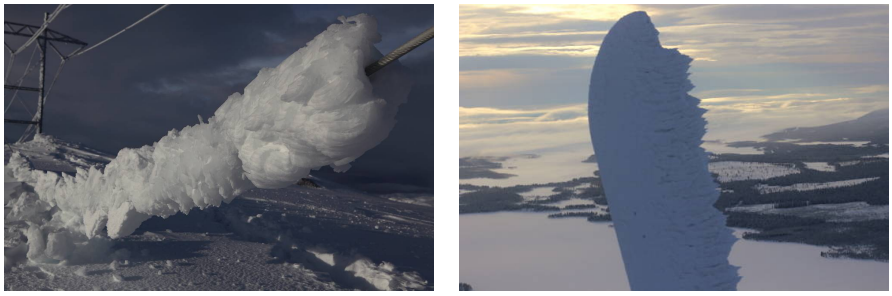

(a) **(b)**

Figure 1.1: Examples of icing on outdoor infrastructure. **(a)** shows the grounded wire of an overhead transmission line that has broken down due to a large ice load[13]. **(b)** shows ice build up on a wind turbine blade[14].

hydrophobic surfaces, which are highly water-repellent surfaces. The concept of hydrophobic surfaces originate from nature, and is particularly evident on the leaves of the Indian Lotus, *Nelumbo nucifera*. Water droplets on the lotus leaves roll off very easily, and can remove dirt and other contaminating particles from the leaves[19]. The origin of the extreme water repellency lies in its surface structure. The surface of the leaves consists of microscale epicuticular wax crystalloids with additional nanoscale structures, shown in figure 1.2. Water will rest on top of these structures and easily roll off. In addition, the wax crystalloids have low surface energy [20], which prevents water from sticking to the surface. Efforts to create hydrophobic surfaces have therefore focused on recreating these two factors: a hierarchical surface roughness on the micro- and nanoscale, in addition to low surface energy.

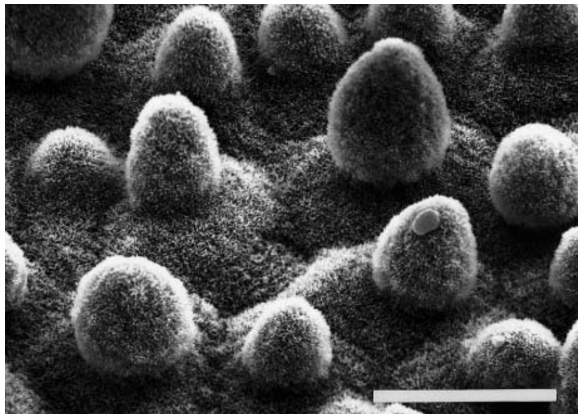

Figure 1.2: A SEM image of the microstructure of the Indian lotus leaf. The bar is 20 µm. Modified from [19].

There are several reasons why hydrophobic surfaces could be used to prevent icing. If supercooled water from freezing rain or atmospheric humidity is prevented from sticking to the surface, icing should theoretically be prevented. Hydrophobic surfaces have demonstrated other beneficial anti-icing properties as well, such as very low freezing temperatures and long delays before water freezes on the surface[21][22]. They have also demonstrated low ice adhesion, which is beneficial for deicing purposes when icing eventually does form in extreme conditions[23][24][25]. However, the origin of these properties are somewhat unclear, and are subject to debate in literature[4][10][12]. Central to the debate is the question of how the properties of a hydrophobic surface relates to its anti-icing properties.

This thesis builds on the work performed by previous master students. Aase Marie Halvorsen[26] and Ellen-Kristin Raasok[27] laid the foundation for the hydrophobic coatings based on fluorosilane sol-gels. They also examined the hydrophobicity and anti-icing properties of the coatings. Raymond Luneng[2] and Ole-Bjørn Ellingsen Moe[3] created hydrophobic surfaces on steel based on Halvorsen and Raasok's findings. They also examined methods to create hierarchical roughness on steel, where Luneng focused on silica nanoparticles, and Ellingsen Moe focused on ZnO nanowires. Finally, Hanna Vassmyr[1] further optimized the deposition method and coating parameters for both the fluorosilane sol-gel and silica nanoparticles. In addition, she refined the methods used to characterize the anti-icing properties of the hydrophobic surfaces.

1.2 Aim of the work

This work aims to expand upon the earlier development of hydrophobic surfaces for anti-icing applications by using aluminium. Some of the most damaging ice accumulation happens on aluminium surfaces, such as on overhead transmission lines and aircraft. The hydrophobicity on Al substrates will be investigated on a hierarchical rough surface covered by a fluorosilane coating. The relationship between hydrophobicity and anti-icing will be investigated.

To accomplish this, aluminium 5052 substrates will be sandblasted with two types of sand to introduce microroughness. Silica nanoparticles will be synthesised and spray coated onto the sandblasted aluminium substrates with varying deposition speeds to create additional nanostructuring on the surface, resulting in a hierarchical roughness. Finally, a fluorosilane-based sol-gel will be synthesised and spray coated onto the substrates to lower their surface energy. The number of coating layers will be varied and its influence on hydrophobic and anti-icing properties investigated. Spray coating will be utilized because it was shown to be a good deposition method for this coating system[1][2]. In addition, it has potential for easy incorporation into existing industries. The end result will be hydrophobic surfaces, with hierarchical roughness and low surface energies.

The hydrophobicity of the substrates will be investigated through measuring their

contact angles and contact angle hystereses, with respect to the sandblasting type, silica particle deposition and number of coating layers. The anti-icing properties will be examined through determining their freezing temperatures, the delay before water freezes and the development in freezing temperature as the substrate is repeatedly cooled and reheated.

Additionally, the contact angle dependence on temperature will be examined, to see if the hydrophobic properties deteriorate at lower temperatures. The substrate micro- and nanostructure will be investigated in detail. Finally, coating durability testing will be performed, to ascertain any influence freezing water had on the coating.

Chapter 2

Theory

2.1 Surface tension

Surface tension is a force which appears for all liquids that have a surface towards a gaseous phase[28, Chapter 6]. The force works to minimize the exposed surface area. It is denoted by γ and expressed in units of N/m. The magnitude of γ is specific for that liquid at a certain temperature. Water, for example, has a reported surface tension of 72.8 mN/m at 20 °C[29].

A tension force also appears when a liquid has an interface to a different system than air. For example, when a water droplet is resting on a solid surface, it will have a certain interaction with the surface. The surface chemistry will decide how energetically favourable the interaction is, and thus the magnitude of the tension force. The surface tension can therefore be said to be a specific case of the more general interfacial tension, which is the tension force between two specific systems.

Another relevant factor when considering the droplet resting on a solid surface is that a pressure difference Δp exists across its surface, because of its curvature[30, Chapter 1].

If the droplet is assumed to have a spherical curvature, the pressure difference Δp is given by the spherical Laplace equation:

$$\Delta p = \frac{2\gamma}{R_s} \tag{2.1}$$

This pressure difference, referred to as the Laplace pressure from here on out, has several consequences. One of them is that the evaporation rate from the curved surface will be larger than for a flat surface. I.e. one would expect a faster evaporation rate for a droplet compared to the same volume with a flat surface.

If work is done against the interfacial tension of a system, energy needs to be expended. For example, increasing the surface area of a volume of water by splitting it in two will have an energy cost. The required work dW needed to increase the surface area by dA can be written as:

$$dW = \gamma dA \tag{2.2}$$

In the context of equation 2.2, γ has a second definition: it is the work per unit area needed to create a new surface. By this definition γ can be expressed in units of J/m^2, and γ is then referred to as surface or interfacial energy.

Of particular interest is the interaction between water and solid surfaces. The interaction depends on the chemical make-up of the surface, i.e. the surface energy γ. Changing γ can change how energetically beneficial it is for water to interact with the surface. One approach to changing γ is to treat the surface with polymers rich in fluorine. Surfaces with a high density of trifluoromethyl-groups ($-CF_3$) has been shown to have extremely low surface energy, and be very water repellent[31]. For example, Heydari et al.[32] treated silicon wafers with 1H,1H,2H,2H-perfluorooctyltriethoxysilane to attain a low surface energy. Its structural formula is shown in figure 2.1.

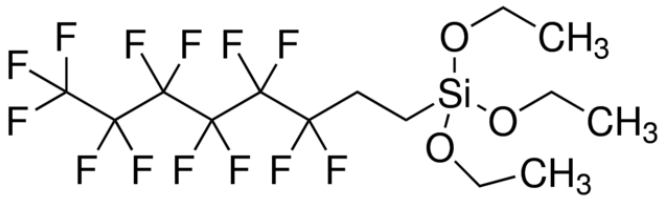

Figure 2.1: The structural formula of 1H,1H,2H,2H-Perfluorooctyltriethoxysilane. Adapted from [33].

2.2 Hydrophobicity

Hydrophobicity (from Greek hydor, meaning water, and phobos, meaning fear) is used to describe the water repellency of a surface. It can be quantified through the contact angle (CA) denoted by θ, which is the angle of contact that water makes with the surface in question. A very hydrophobic surface results in a higher contact angle, as water seeks to reduce its contact area with the surface. Inversely, a less hydrophobic surface gives a lower contact angle. Typically, a hydrophobic surface is defined as having $\theta > 90°$, while $\theta < 90°$ for a hydrophilic surface[5]. The two cases are illustrated in figure 2.2.

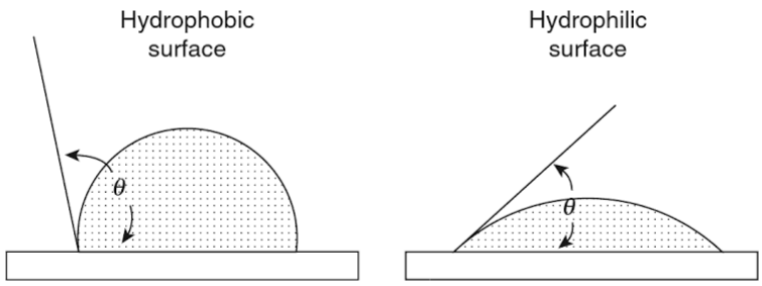

Figure 2.2: An illustration of the static contact angle θ for a droplet resting on a hydrophobic (left) and a hydrophilic (right) surface respectively. Adapted from [34].

For a water droplet resting on a surface, the contact angle is a result of the three media in the system interacting: the solid surface, the liquid water and the water vapour. The angle appears on the solid-liquid-vapour three-phase contact line, and varies quantitatively based on the interfacial tensions between each of the three media[35]. The exact relation is given by Young's equation:

$$\cos\theta = \frac{\gamma_{sv} - \gamma_{sl}}{\gamma_{lv}} \tag{2.3}$$

where γ_{sl}, γ_{sv} and γ_{lv} are the interfacial tensions between solid and liquid, solid and vapour, and liquid and vapour respectively[12][35]. Young's equation is therefore effectively a force balance equation, as illustrated in figure 2.3.

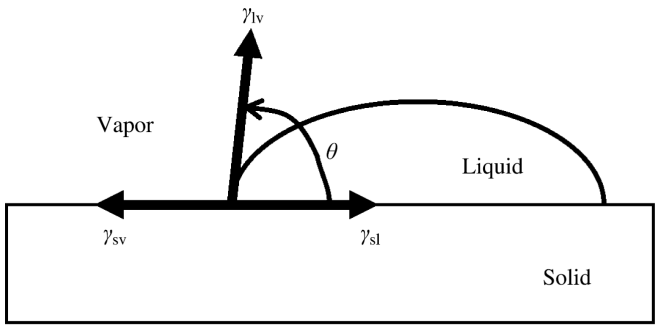

Figure 2.3: Illustration of Young's equation. The interfacial tensions between the three media in the system are noted as γ_{sl}, γ_{sv} and γ_{lv}. They work as forces denoted by vectors, creating a force balance and giving rise to the contact angle θ. Adapted from [5].

Young's equation was proposed in 1805 by Thomas Young[36], and is widely used in surface science to this day[28]. It should be noted however that despite its

widespread use, several major assumptions are made in the derivation of equation (2.3). Perhaps the biggest assumption is that the surface is perfectly smooth. Since this is not the case for most real world surfaces, the influence of roughness on contact angles will be investigated further.

2.2.1 Influence of roughness

Most solid surfaces have some amount of roughness despite appearing smooth. This roughness can have micro- and nanometer sized features, often both. The roughness created on surfaces is normally unintentional, for example through the process in which the surface is fabricated. It can also be created intentionally, for example by sandblasting the surface. This roughness can have a large effect on the contact angle and hydrophobicity[37]. Increasing the roughness of a hydrophobic surface will make it even more hydrophobic, and vice versa for a hydrophilic surface. That means to make an extremely hydrophobic surface, a low energy surface must be combined with a certain surface roughness. More specifically, a hierarchical surface roughness is sought after to maximize the hydrophobicity, combining micrometer and nanometer sized surface features[4][38][39].

In the case of the aluminium surface, several approaches have been taken to create a hierarchical surface roughness upon it. Cho et al.[40] reports using a combination of sandblasting techniques and alkali surface modification to create such a surface. They used sandblasting to create a microstructured aluminium surface, and immersion in a NaOH solution to create a nanostructure with flake-like morphology. They then applied a self-assembled monolayer fluorosilane coating to lower the surface energy. A different approach is taken by Shi et al.[41]. They deposited nano-silica particles onto acid-etched aluminium surfaces in order to create hierarchical roughness. They then coated the surface with a fluorosilane to make it hydrophobic. Jung et al.[10] synthesised polymer coatings with added poly(tetrafluorethylene) (PTFE) nanoparticles and spray coated it onto smooth and sandblasted aluminium surfaces to create hydrophobic surfaces.

The Cassie-Baxter model and Wenzel model are commonly used in literature to understand the contact angle of droplets on rough surfaces. These models offer two different takes on how a liquid can be in contact with a surface. In the Wenzel model, the liquid is assumed to be fully in contact with the surface, with no air pockets[42]. It is illustrated in figure 2.4. In this case, the apparent contact angle θ^* can be found through the relation:

$$\cos(\theta^*) = r\cos(\theta) \tag{2.4}$$

where r is a roughness factor which describes the ratio of actual surface area to the projected area.

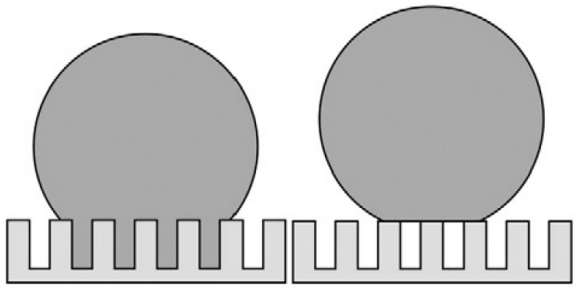

Figure 2.4: Illustration of the Wenzel (left) and Cassie-Baxter (right) contact modes respectively. Modified from [4].

The Cassie-Baxter model is a contact model originally developed for the wetting of porous surfaces[43]. The model can be applied to a droplet resting on top of the surface features of a rough, hydrophobic surface. In this case, there are air pockets trapped under the droplet, in contrast to the Wenzel model. The Cassie-Baxter contact mode is illustrated in figure 2.4. The contact mode is more typically encountered for surfaces which have been chemically treated to lower surface energy and to promote hydrophobicity[30]. For the Cassie-Baxter contact mode, the apparent contact angle θ^* is given by the equation:

$$\cos(\theta^*) = -1 + \Phi_S(\cos(\theta) + 1) \tag{2.5}$$

where Φ_S is the surface fraction that is in contact with the liquid.

Equation (2.5) shows that the observed contact angle θ^* in the Cassie-Baxter regime will be much larger than on a smooth surface, as long as θ is larger than 90°. In fact, having a rough surface is absolutely necessary to achieve contact angles above 120°[38]. It is worth noting that θ^* in equation (2.5) changes drastically if Φ_S is varied, especially if Φ_S gets very small. This contributes to the difficulty of creating surfaces with consistently high contact angles. Equation (2.5) also shows that a contact angle of 180° is unrealisable, because Φ_S can never reach zero. Nevertheless, the Cassie-Baxter equation makes it clear that promoting air trapping through reducing Φ_S is important in increasing contact angles [30, pp. 222-223].

Quéré[38] discusses how to determine whether a droplet will prefer the Wenzel- or Cassie-Baxter mode. By comparing the surface energy of a droplet in each state, he concludes that the Cassie-Baxter mode will be observed when $\theta > \theta_c$, where:

$$\cos(\theta_c) = -\frac{1 - \Phi_s}{r - \Phi_s} \tag{2.6}$$

Here, Φ_s is the surface fraction from equation (2.5), and r is the roughness factor from equation (2.4).

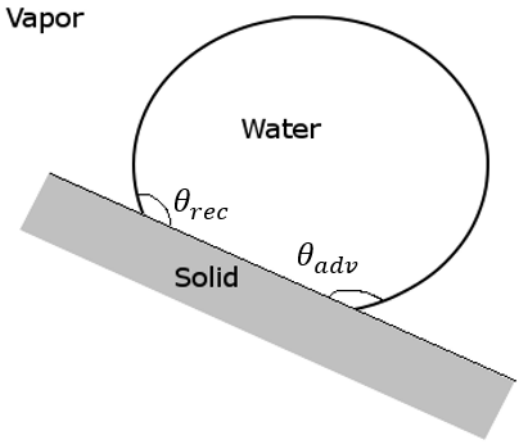

Figure 2.5: A droplet resting on a tilted, solid surface. θ_{adv} is the advancing contact angle. θ_{rec} is the receding contact angle.

A droplet does not have to exist only in the Wenzel- or Cassie-Baxter contact mode. In fact, a coexistence of states is possible. The Cassie-Baxter mode can also be metastable, and a transition to the Wenzel mode can occur if it is more energetically beneficial. The transition can for example be triggered by pushing the droplet into the surface with a certain force[38]. In this case, the droplet can be partly impaled by the surface asperities[44].

2.2.2 Contact angle hysteresis

Another important parameter used in determining the hydrophobicity of a surface is the contact angle hysteresis (CAH). Consider a droplet which is deposited on a tilted surface, illustrated in figure 2.5. The advancing contact line of the droplet pointing down the slope will typically have a larger contact angle compared to the level one, this is the advancing contact angle. Initially, the contact line of the droplet will be pinned to the surface as it is deposited. It will be impossible to move the droplet unless a certain macroscopic force is applied[30, p. 71]. But if the surface tilt increases, the gravity of the droplet might eventually overcome the pinning. The advancing contact angle will keep increasing until a certain value, until the advancing contact line moves. This maximum value is known as the advancing contact angle, or θ_{adv}. Inversely, the receding contact line trailing the droplet will have a smaller contact angle. When the surface is tilted, the angle will keep decreasing until the contact line moves, giving the minimum receding contact angle θ_{rec}[12][45, pp. 159-160]. The contact angle hysteresis is given by the difference between the advancing and receding contact angle:

$$CAH = \theta_{adv} - \theta_{rec} \tag{2.7}$$

CAH is present for most surfaces, and can be seen as an expression of the non-ideality of the surface[35][46]. A higher CAH is typically indicative of larger adhesion forces between droplet and surface. However, a surface can exhibit large CAH while at the same time maintaining large static contact angles. An example of such a surface is the rose petal surface[47]. Properly characterizing the hydrophobicity of a surface therefore necessitates not only finding its static contact angles, but also its CAH.

Growing interest has been shown in superhydrophobic surfaces in literature[37] [48][49]. Superhydrophobic surfaces exhibit not only a CA above 150°, but also a CAH of less than 10°[4]. Droplets on these surfaces will roll off at very low tilting angles, and they will have excellent self-cleaning abilities. There are several examples of such surfaces in nature, and the lotus plant leaves is an often used example.

The key behind achieving a superhydrophobic surface is related to exploiting the Cassie-Baxter contact mode. As a droplet rests on top of the features of a rough surface, its only adhesion to the surface will be at these areas. The total water/solid surface area will be very low, and thus the total adhesion will be lower as well. Quéré[37] writes that in the case of strong pinning on dilute defects, the hysteresis can be related to the defects per unit area ϕ_s:

$$(\cos\theta_{rec} - \cos\theta_{adv}) \approx \phi_s \log(1/\phi_s) \tag{2.8}$$

That means minimizing CAH requires minimizing the density of defects that the droplets rests upon. However, the density of defects still has to be large enough to support the droplet such that the Cassie-Baxter mode is maintained. In addition, the pinning force of the droplets to the defects can be lowered by reducing the surface energy. That makes it necessary to combine a certain surface roughness with low surface energy in order to achieve a superhydrophobic surface.

A closely related parameter to the CAH is the roll off angle (ROA), which is reported in literature as its own parameter[5][35]. Take a sessile droplet resting on a tilted surface, as shown in figure 2.5. The ROA is the tilting angle at which the droplet starts to roll or slide down, typically during CAH measurements. A low ROA is reported to imply a low CAH as well, but they are not equal[48].

Evaporation and contact angle

It is important to note that a droplet resting on a surface is a dynamic system. For example, the droplet can evaporate, which may change its apparent contact angle. This phenomenon has been well studied in literature. Birdi, Vu and Winter[50] found

that the evaporation led to a constant volume decrease over time, depending on droplet size. Another study was performed by Bourges-Monnier and Shanahan[51]. They found that initially, the diameter of a deposited droplet stayed constant while it evaporated. However, both the height of the droplet and its contact angle decreased. The contact line of the droplet was pinned, which ensured a constant surface area between droplet and surface. The contact line pinning thus led to the reduction of the contact angle during evaporation. This lasted until a certain contact angle was reached, when the contact line started to recede. This angle was interpreted by the authors to be the receding contact angle. Kulinich and Farzaneh[52] writes that with a low enough CAH, the contact line pinning will be weak. In that case, the CA will remain relatively constant during evaporation, but the contact diameter will decrease.

2.3 Anti-icing

Several different groups publicized results between 2009 and 2010 showing very beneficial anti-icing properties of some hydrophobic surfaces. For example, in 2009, Tourkine et al.[53] reported a significant delay before droplets froze on superhydrophobic surfaces holding $-8\,^{\circ}\mathrm{C}$. Kulinich and Farzaneh[24][54] reported a correlation between ice adhesion strength and CAH in 2009. Cao et al.[55] reported low ice accretion and reduced nucleation of supercooled water on a hydrophobic surface in 2009. In 2010, Wang et al.[56] reported reduced ice accretion on hydrophobic surfaces. These findings, amongst others, prompted a discussion between several authors if hydrophobic or superhydrophobic surfaces could be used to prevent ice nucleation on surfaces, or lower ice adhesion[4][12][57][58]. They concluded that the earlier results cannot be seen as conclusive evidence for a general correlation between hydrophobicity and anti-icing properties. One has to consider how each aspect of a hydrophobic surface affects each separate anti-icing property to properly evaluate any correlations.

The anti-icing performance of a surface can be evaluated using two different metrics: the ice nucleation temperature and the time delay before ice nucleation on the surface[59]. There has also been interest in the ice adhesion strength on hydrophobic surfaces in literature. The term icephobicity has been used to encompass either or all of these traits by different authors[58]. However, in this work, icephobicity will strictly refer to low ice adhesion, while the general term anti-icing will refer to the ability of a surface to prevent icing in the first place. The ice adhesion strength will be considered outside the scope of this work. As such, this work will consider how the hydrophobicity of a surface is related to the two anti-icing properties.

2.3.1 Hydrophobicity and anti-icing

Several groups have found that some hydrophobic surfaces can supress or significantly delay ice nucleation[22][59][60]. Most authors generally attribute this effect

to the following three phenomena[12]:

1. An insulating layer of air formed under droplets in the Cassie-Baxter contact regime
2. Reduced contact area between solid and liquid
3. An increase in the free-energy barrier to heterogeneous nucleation

Regarding the first and second explanation, if a droplet is resting on a surface in the Cassie-Baxter contact regime, air may be trapped under the droplet. The air will be contained within the asperities of the surface, reducing the water/solid surface area. The water/air interfacial area may be as much as 10-100 times larger than the water/solid area, depending on the surface topography[53]. The air layer will function as a thermal insulator, leading to a lower heat transfer rate from droplet to solid[61]. If the solid is gradually cooled at a constant rate, then the droplet will cool at a reduced rate compared to the solid. Lower nucleation temperatures and longer freezing delay times will be observed as a result. This effect may help explain some of the observed ice suppression effects observed in literature.

The third explanation of the ice nucleation delay concerns the thermodynamics of nucleation. When a water droplet freezes, it has to overcome a certain critical energy barrier for homogeneous nucleation, or the free-energy barrier. This energy barrier ΔG^*_{homo} can be expressed as[61]:

$$\Delta G^*_{homo} = \frac{16}{3} \frac{\pi \gamma^3_{AB}}{[(\frac{\Delta T}{T_m})\Delta H_f]^2} \tag{2.9}$$

Here, γ_{AB} is the surface tension between water and ice, ΔT is the difference between the actual temperature and melting temperature, T_m is the melting temperature and ΔH_f is the latent heat of fusion. Equation (2.9) shows the absolute maximum energy barrier which is required for water to spontaneously nucleate, i.e. the critical energy barrier for homogeneous nucleation. However, ΔG^*_{homo} can be reduced by factors such as vibration and contaminants. If the water rests on a solid surface, any surface defects may also reduce the critical energy barrier. In these cases it will undergo heterogeneous nucleation. The energy barrier ΔG^*_{homo} will be modified by a reducing factor f, which ranges from 0 to 1. The heterogeneous nucleation energy barrier ΔG^*_{hetero} is then given by:

$$\Delta G^*_{hetero} = \Delta G^*_{homo} f \tag{2.10}$$

f is a function of the roughness radius of curvature R_s, the water static contact angle θ, several interfacial energy terms and the critical ice nucleus radius r_c. r_c is 9.1 nm at $-5\,^\circ$C and 4.5 nm at $-10\,^\circ$C[32]. Assuming that R_s is greater than $10r_c$, then f can be expressed as[60]:

$$f = \frac{1}{4}[2 + (\frac{\gamma_{iv} - \gamma lv}{\gamma_{il}})\cos\theta][1 - (\frac{\gamma_{iv} - \gamma lv}{\gamma_{il}})\cos\theta]^2 \tag{2.11}$$

where γ_{iv}, γlv and γ_{il} are the interfacial energies between ice and vapour, water and vapour, and ice and water respectively.

The interfacial energy term in equation (2.11) will vary with temperature, but will stay at approximately unity for the temperature range most relevant here[10][29] [62].

Then, the heterogeneous energy barrier ΔG^*_{hetero} becomes:

$$\Delta G^*_{hetero} = \Delta G^*_{homo} f = \Delta G^*_{homo} \frac{1}{4}(2 + \cos\theta)(1 - \cos\theta)^2 \tag{2.12}$$

as given by Oberli et al.[61] and Bahadur et al.[63].

Equation (2.12) implies that as the contact angle $\theta \to 180°$, then $f \to 1$ and the heterogeneous energy barrier approaches the homogeneous barrier, $\Delta G^*_{hetero} \to \Delta G^*_{homo}$. Based on this, it is clear that maximizing the contact angle with water would be the best approach to limit ice nucleation. However, some groups have publicized results which seem to conflict with this picture. Jung et al.[10] found a larger freezing delay on hydrophilic surfaces with nanoscale roughness, compared to the hydrophobic surfaces they tested. Some authors have tried to explain this discrepancy by arguing that only the local surface energy where the ice nucleus is in contact with the solid is important, rather than the macroscopic surface energy[32]. In this case, f becomes a function of the CA of the ice nucleus in that point. Furthermore, a quasi-liquid layer has been postulated to exist between the ice nucleus and the solid surface[21][59]. This is illustrated in figure 2.6. In that case, the macroscopic CA used in equation (2.12) should be replaced with θ_{IW}, which is the CA between the ice embryo and its quasi-liquid layer.

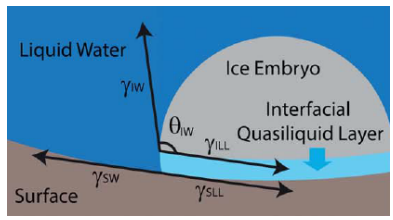

Figure 2.6: An illustration of an ice embryo on a solid surface, resting on a quasi-liquid boundary layer. Adapted from [59].

As the origin of the nucleation delay is not entirely clear, there have also been disagreements on which parameters to optimize for the hydrophobic surfaces. Some

groups have focused on the nucleation delay on microstructured surfaces[63], while others have found the nanostructuring to be more important[59]. It has also been been proposed that surfaces with minimal roughness are beneficial when condensation and frost formation can occur[10][64].

Kreder et al.[12] explains this wide variance in results from different groups with the complexity of the system. Several length scales are involved when considering the nucleation of ice on a surface: the critical nucleus size for ice (<10 nm), the nanoscopic surface roughness (<100 nm), the topography needed for superhydrophobicity (50 nm to 10 µm) and the macroscopic droplet dimensions. The wide variety of hydrophobic surfaces tested for anti-icing properties also have a wide variety of topographies on different length scales. Other complicating factors include the effect of opportunistic nucleation sites on a surface, droplet impurities, surface chemistry and environmental conditions. Although one group can keep their experimental parameters consistent, these factors make comparing results across literature more challenging.

2.4 Sol-gel method

The sol-gel method is a synthesis route based on polymerization which is used to create a wide range of functional materials[65][66]. The method can produce ceramic materials with high purity, with the potential for very different structures and compositions[67]. The sol-gel method is based on using certain inorganic or metal-organic precursors, which are the starting compounds of the synthesis[68][69]. These precursors typically consist of a metal or metalloid element and certain non-metallic ligands, or appendages. One example of a precursor is the commonly used tetraethyl orthosilicate (TEOS), $Si(OC_2H_5)_4$, which is a metal alkoxide. The structural formula of TEOS is shown in figure 2.7.

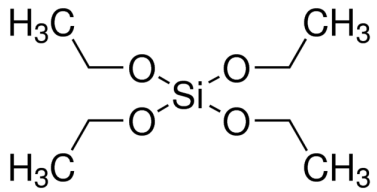

Figure 2.7: The structural formula of tetraethyl orthosilicate (TEOS). Adapted from [70].

For TEOS, the central metalloid, Si, is bound to four $-OC_2H_5$ ligands. TEOS and other metal alkoxides react readily with water, whereby one of its ligands is displaced through hydrolysis:

$$\equiv Si{-}OR + H_2O \rightleftharpoons \equiv Si{-}OH + ROH \tag{2.13}$$

Here, $-\mathrm{OR}$ is the generalized form of a ligand bound to the central metalloid, in this case Si. The hydrolysis in equation 2.13 may continue partially or fully, depending on the presence of water or catalysts, which will displace more ligands. The hydrolyzed precursors may then react through one of two condensation reactions:

$$\equiv\mathrm{Si}-\mathrm{OH} + \mathrm{HO}-\mathrm{Si}\equiv \rightleftharpoons \equiv\mathrm{Si}-\mathrm{O}-\mathrm{Si}\equiv + \mathrm{H_2O} \tag{2.14}$$

$$\equiv\mathrm{Si}-\mathrm{OR} + \mathrm{HO}-\mathrm{Si}\equiv \rightleftharpoons \equiv\mathrm{Si}-\mathrm{O}-\mathrm{Si}\equiv + \mathrm{ROH} \tag{2.15}$$

Equations (2.14) and (2.15) form the basis for the sol-gel method. The precursor molecules are bound together through a polymerization process, potentially creating large networks. The structures of the resulting networks can be carefully controlled through several parameters, which will be expanded upon in section 2.4.2.

2.4.1 Steps in the Sol-gel process

The sol-gel process can be divided into six steps[71]:

1. Formation of a stable solution (a sol) of the precursor compound.
2. Gelation resulting from the precursor molecules reacting through equation (2.14) and (2.15), forming a network.
3. Aging of the gel (syneresis) where the condensation reactions continue, eventually forming a solid mass with contraction of the network.
4. Drying of the gel, which happens as water and other solvents are expulsed from the network.
5. Dehydration of the sol, where the structure is calcined to remove surface $-\mathrm{OH}$ groups.
6. Densification and decomposition of the gel at high temperatures ($>800\,^{\circ}\mathrm{C}$).

Depending on the desired structure and application, some of these steps may be omitted. For example, if a thin sol-gel coating is desired, dehydrating the coating at high temperatures would cause undesirable shrinking and cracking, and is therefore skipped.

2.4.2 Influencing the network structure

Two important parameters in the initial sol can be changed to control the final network structure: water content, and the pH in solution. Regarding the water content in solution, it has been shown how the precursor hydrolyses using water in

equation (2.13). The water content in the sol will decide the degree of hydrolysis, if it is partial or total. The degree of hydrolysis will control the morphology and structure formed by condensation, through equation (2.14) and (2.15).

The pH in solution will also help determine the final structure. H_3O^+ and OH^- groups in solution can help catalyse the hydrolysis and condensation reactions respectively. At lower pH, the rate of hydrolysis will increase, making it the dominant reaction. The increased hydrolysis will promote the formation of linear Si−O−Si chains, with cross-linking and branching happening later during the aging step. Inversely, at higher pH, the condensation reaction rate will increase. A greater degree of cross-linking will be promoted early on, leading the monomers to form agglomerates. The agglomerates may eventually cross-link, creating a network structure.

One application of the sol-gel method is to make a variety of functional coatings on surfaces. The morphology and structure of a coating will change depending on the water content and pH. An acid-catalysed sol-gel will result in a dense, thinner coating, as the linear chains align during the coating deposition. Contrarily, a base-catalysed sol-gel will make a thicker coating, with a rougher surface because of its agglomerate structure.

2.4.3 Silica nanoparticle synthesis

The Stöber-Fink-Bohn-method (SFB-method) is a widely used method of generating a monodisperse suspension of SiO_2 nanoparticles[72]. Spherical particles in the size range of 5 nm to 2000 nm with homogenous size distribution can be produced[73]. The method is based on reacting TEOS with water, using ammonia as a catalyst and an alcohol with low molecular weight as solvent. The TEOS will hydrolyse according to equation (2.13) to form the singly hydrolysed $(OC_2H_5)_3Si(OH)$. This monomer will further react according to the following simplified condensation reaction:

$$(OC_2H_5)_3Si(OH) + H_2O \rightleftharpoons SiO_2 + 3\,C_2H_5OH \tag{2.16}$$

The SFB-method has similarities to the sol-gel method in that silicon alkoxide precursors react through hydrolysis and condensation to form a structure. However, letting the reaction progress under the specific conditions that the SFB-method demands results in spherical SiO_2 particles and not a gel. A general explanation for this phenomenon is that the molar ratio of water to TEOS used is much higher than strictly necessary for the total hydrolysis and condensation reactions. The large water content in addition to the high pH serves to promote condensation. Thus compact network structures are favoured rather than a gel[68].

Several explanations for the growth mechanism behind the SiO_2 particles, or silica particles, have been proposed. Masalov et al.[74] categorizes them into two types. The first is the monomer addition growth model. First proposed by LaMer et

al. in 1950[75], the model attempts to explain the growth mechanism inspired by classic nucleation theory. Reaching a certain supersaturation of monomers triggers nucleation and growth through continued diffusion of monomers to the nucleus surface. However, as Brinker and Scherer[68] point out, this view conflicts with the sometimes porous structure of the spheres. They explain that the smaller silica spheres are porous, with reducing porosity as they grow larger. Another issue with the model is its explanation of the narrow size distribution of the particles. It attempts to explain the size distribution as a consequence of a very short time spent above the critical nucleation concentration of reaction precursors. However, Bogush and Zukoski[76] found that the concentration of reaction precursors stay above the concentration required for nucleation to occur for an extensive time period.

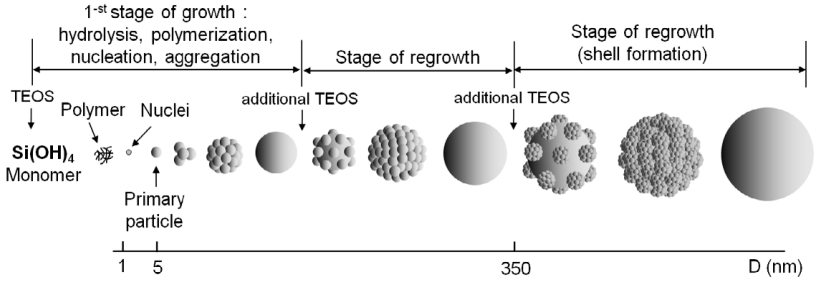

Figure 2.8: An overview of the proposed growth model for silica particles grown by the SFB method. From [74].

The second growth model is the aggregation growth model. Here, nanometer-sized particles aggregate to form larger particles. Later, depending on the reaction conditions, the growth mode changes to the condensation of monomeric and dimeric silicates on the surface. They therefore end up with a hard outer silica shell, and porous inner structure, seemingly in agreement with observed experimental results. Masalov et al.[74] proposes another growth mechanism based on the two existing models and experimental data, which is summarized in figure 2.8. Essentially, it is a multistage particle growth model based on particle aggregation. When the concentration of the hydrolysed silica monomers decrease, the growth transits to mono- and dimer addition to the particle surfaces. With the addition of more TEOS to the solution, new and smaller secondary particles are formed, and will start to grow. When around 30 nm to 40 nm in size, the secondary particles will join to the surface of the larger, primary particles. The growth will again start to transit to mono- and dimer addition to the particle surface, creating the smooth shell. This process can continue several times with addition of more TEOS.

2.5 Spray coating

Spray coating is a technique used for depositing solutions onto surfaces. It consists of forcing the solution through a nozzle by applying pressurized gas. The surface

to be coated can be positioned on a hot plate to aid in evaporation of solvents[77]. Spray coating is a highly scalable and flexible deposition method used for several different applications, such as in the manufacturing of hydrophobic surfaces. For example, Li et al.[78] used spray coating to coat glass insulators used for high voltage transmission lines with a PDMS/modified nano-silica hybrid system. This resulted in very hydrophobic surfaces and significant reduction in ice accumulation. Shang, Zhou and Xiao[79] used spray coating to apply a suspension of silica microsphere and silica sol onto a glass substrate. The suspension was used to attain a micro/nanoscale hierarchical roughness upon the surface. The surface was later treated with 1H,1H,2H,2H-perfluorodecyltriethoxysilane to attain a hydrophobic surface.

Chapter 3

Experimental

Figure 3.1 shows a flowchart of the experimental work that was performed. Each point is further detailed in the following sections.

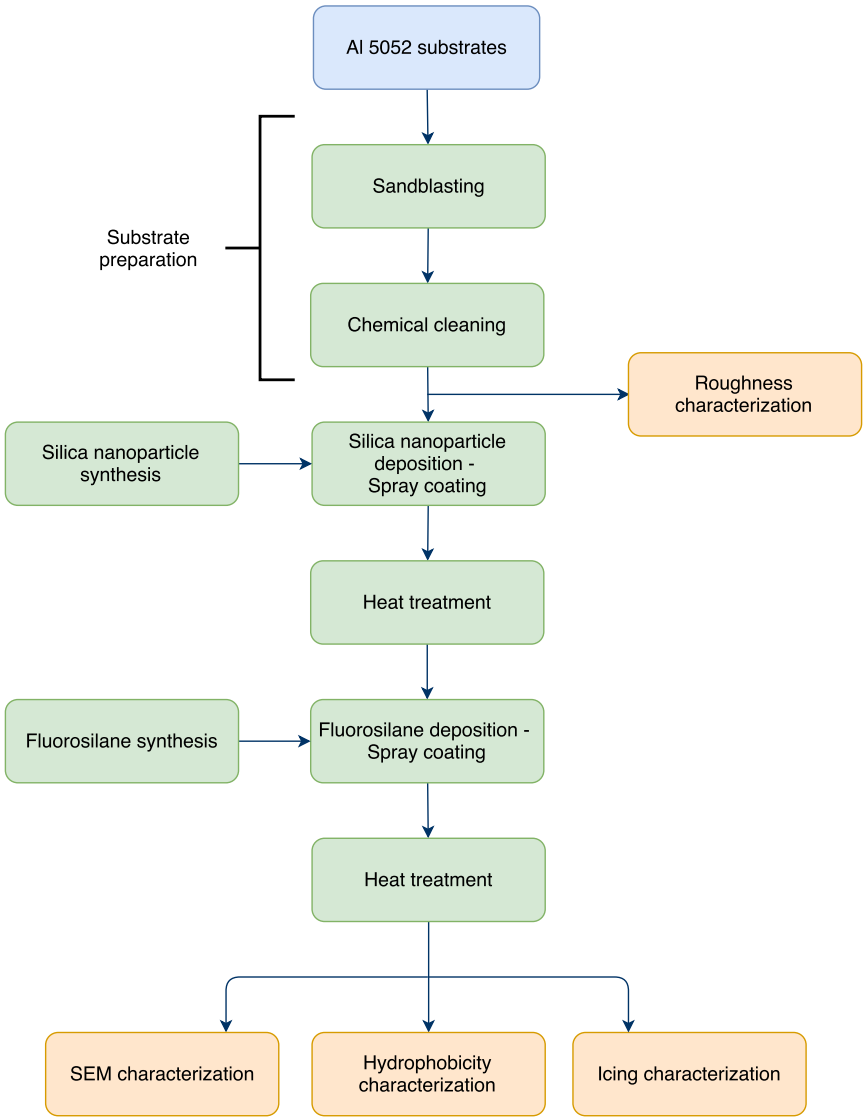

Figure 3.1: A flowchart of the experimental work. The blue bubble show the starting substrate, green bubbles show manufacturing steps, while orange bubbles show characterization steps.

3.1 Substrate details

Aluminium substrates of the 5052 type were used, hereby referred to as Al substrates. Their dimensions were 1 cm × 1.5 cm × 0.2 cm. The substrates were delivered by NTNU Fine Mechanical Workshop.

3.2 Preparation of substrates

3.2.1 Sandblasting of substrates

Aluminium substrates were sandblasted to introduce microroughness in the surface. The substrates were sandblasted in a sandblasting machine property of SINTEF. Two types of sand were used, with different grain sizes. The first type of sand used was SiO_2, with a grain size of approximately 150 µm. This type of sand will be referred to as "fine" from here on out. The second type was Al_2O_3 with a grain size of 0.5 mm to 1 mm, this type will be referred to as "coarse". The machine was thoroughly cleaned with pressurized air between sandblasting runs to avoid contamination. When sandblasting, each substrate had their backside fastened with duct tape to a wooden support inside the machine. The substrates were then blasted with sand for approximately five seconds each. The sand ejection speed from the nozzle was unknown.

3.2.2 Chemical cleaning

To ensure no organic residue or other contamination was left on the substrates, a chemical cleaning procedure was performed. This was performed after the sandblasting step. The substrates were immersed in acetone, then isopropanol and finally ethanol, spending 5 minutes in each solution. They were then left to evaporate for approximately 10 minutes.

3.3 Roughness measurements of sandblasted substrates

The average roughness of the sandblasted Al substrates were measured using a Veeco Dektak 150 Profilometer at the NTNU NanoLab. The average roughness was measured by the parameter R_a, which is the arithmetic average of the deviation from a level baseline of each point on the surface. The baseline was set by using a flat aluminium substrate which was not sandblasted. Most of the roughness tests were conducted over 4 mm of substrate each time, using 180 s per measurement. Some roughness measurements were performed over a smaller distance (2 mm over

150 s), or over a larger area and duration (8 mm over 200 s). 4 substrates were measured upon.

3.4 Synthesis of the silica nanoparticle sol

The SiO_2 (silica) nanoparticles were synthesised through the sol-gel method, using tetraethyl orthosilicate (TEOS) as a precursor molecule. The synthesis method used was adapted from earlier master theses[1][2], based on the Stöber-Fink-Bohn process[72]. Figure 3.2 shows a picture of the experimental setup.

The chemicals used are summarized in table 3.1. First, ethanol, DI water and ammonium hydroxide were mixed for a minute in a round bottom flask. Then, TEOS was added drop-wise to the flask across a timespan of 3 minutes. The solution was then left for 1 hour. Afterwards, the solution was transferred to a new container, and allowed to cool to room temperature. Unused solution was stored in a fridge at 5 °C, though care was taken not to use any old solution at a later time with visible agglomeration and precipitation.

Table 3.1: Overview of the chemicals used for the silica particle sol synthesis.

Chemical	Formula	CAS	Volume [mL]	Purpose
Tetraethyl orthosilicate	$Si(OC_2H_5)_4$	78-10-4	0.75	Silica sol precursor
Ethanol	C_2H_6OH	64-17-5	22.5	Solvent
Ammonium hydroxide solution (28-30%)	$NH_4OH(aq)$	1336-21-6	1.5	pH regulation and catalyst
DI water	H_2O	7732-18-5	2.5	Reactant

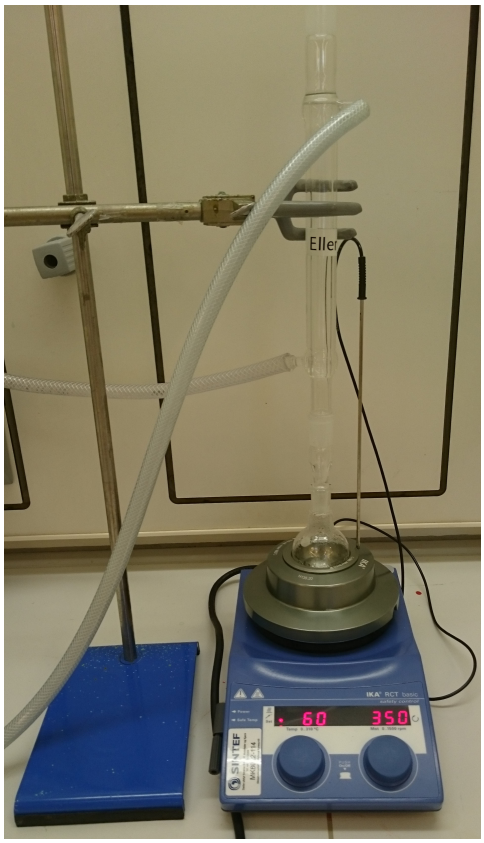

Figure 3.2: A picture showing the experimental setup used for synthesising silica nanoparticles and fluorosilane sol-gel. The synthesis was performed in a 50 mL round bottom flask on a combined hot plate and magnetic stirrer. For the silica nanoparticles, the hotplate was kept at 35 °C with the magnetic stirrer rotating a stir bar in the solution at 300 rpm. For the fluorosilane sol-gel, the hotplate was kept at 60 °C with a magnetic stir bar rotating at 350 rpm. A Liebig condenser was used above the round bottom flask to avoid solvent loss due to evaporation. The condenser was connected via tubing to a water outlet.

3.5 Synthesis of the fluorosilane sol-gel

The fluorosilane sol-gel synthesised in this work used 1H,1H,2H,2H-perfluorooctyl-triethoxysilane as a precursor molecule, its structural formula is shown in figure 2.1. The synthesis parameters were based on the previous master's theses on this subject[1][2]. Figure 3.2 shows the experimental setup used for synthesising the fluorosilane sol-gel. The reagents used, as well as their purpose and the amounts used, is summarized in table 3.2. The 0.070 mL of DI water added to the synthesis held a pH of 10, to ensure a base-catalyzed sol-gel reaction. Creating a solution of DI water with a pH of 10 was accomplished by slowly adding NH_4OH to the solution until its pH reached 10. As 0.070 mL of this solution was added, only 2.71×10^{-6} mL of NH_4OH was added to the synthesis in total.

Table 3.2: Overview of the chemicals used for the fluorosilane sol synthesis.

Chemical	Formula	CAS	Volume [mL]	Purpose
1H,1H,2H,2H-Perfluorooctyl-triethoxysilane	$C_{14}H_{19}F_{13}O_3Si$	51851-37-7	0.5	Fluorosilane sol precursor
Ethanol	C_2H_6OH	64-17-5	3.043	Solvent
Ammonium hydroxide solution (28-30%)	NH_4OH(aq)	1336-21-6	2.71×10^{-6}	pH regulation and catalyst
DI water	H_2O	7732-18-5	0.070	Reactant

The synthesis was carried out by first adding the ethanol and pH adjusted DI water to the round bottom flask. Then, the fluorosilane sol precursor was added to the flask. The solution was left to react for 1 hour. Afterwards, the solution was transferred to another container, and allowed to cool to room temperature for 1 hour. It was then used to coat substrates. Unused solution was stored in a fridge holding 5 °C.

3.6 Sol deposition via spray coating

Both the silica nanoparticle sol and the fluorosilane sol was deposited onto substrates using spray coating. The coating was performed in an ExactaCoat SC spray coater from Sono-Tek, pictured in figure 3.3. Each substrate was fastened inside the spray coater using double sided tape on aluminium foil fastened to the deposition platform. The platform could be heated, allowing for faster evaporation of solvents. A computer program controlled the position and speed of the spray nozzle, allowing

for multiple layers. The speed of the nozzle was set to a constant 40 mm/s. The nozzle moved across the substrates in straight lines, with 3 mm spacing between them. Because of the spray width of the nozzle, this resulted in a certain amount of overlap between the lines.

Figure 3.3: The ExactaCoat SC spray coater used for spray coating substrates and accompanying computer.

3.6.1 Silica deposition

For the deposition of the silica nanoparticles, an ultrasonic syringe was used, to help prevent agglomeration. The deposition speed used was primarily 1 mm/min, with 0.5 mm/min being used for certain substrates to investigate any effects a reduced deposition of silica particles would have on its hydrophobicity and anti-icing properties. Only a single layer was deposited. The deposition platform was kept at 50 °C. Some substrates were also not coated with silica particles at all to further investigate its effects.

3.6.2 Fluorosilane deposition

The fluorosilane sol was diluted at a 1:1 volume ratio with ethanol, using a magnetic stirrer rotating at 350 rpm for 10 minutes. The number of layers deposited varied from 1 to 4 layers to find the optimal thickness. The spray coater deposition surface was heated at 50 °C. The heating was used to accelerate the evaporation of solvents between layers. Each new substrate spent a minimum of 5 minutes fastened to

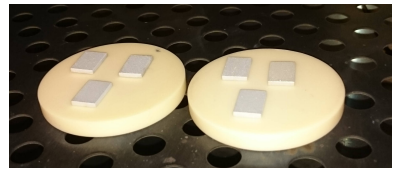

Figure 3.4: A picture showing how a batch of substrates were oriented in the Carbolite oven.

the surface to heat it before coating. There was a 1 minute interval between each coating layer to facilitate the evaporation.

3.7 Heat treatment

The substrates were heat treated after each deposition step to remove any remaining solvents and water. The heat treatment was done in a programmable Carbolite HTCR6/28 oven approximately 15-30 minutes after deposition.

After deposition of the silica sol, the substrates were heat treated at 100 °C. The temperature was ramped up from 25 °C at a rate of 100 °C/h. The ramp down speed was set to the same as the ramp up speed, but turned out to be considerably slower in practice. The substrates were therefore manually retrieved after 3 hours and 30 minutes total, with the oven holding 82 °C.

After deposition of the fluorosilane sol, the substrates were heat treated at 150 °C. The temperature ramp up was from 25 °C at a rate of 100 °C/h, with the ramp down set to the same rate. The substrates were retrieved after 6 hours and 30 minutes.

A picture of the orientation of substrates in the oven is shown in figure 3.4.

3.8 Overview of samples

Table 3.3 show an overview of all the substrate samples prepared. The three most important parameters that were varied for each sample are shown. The designated name of each sample contains each of the three parameters that were varied, and an explanation of the naming system is shown in figure 3.5.

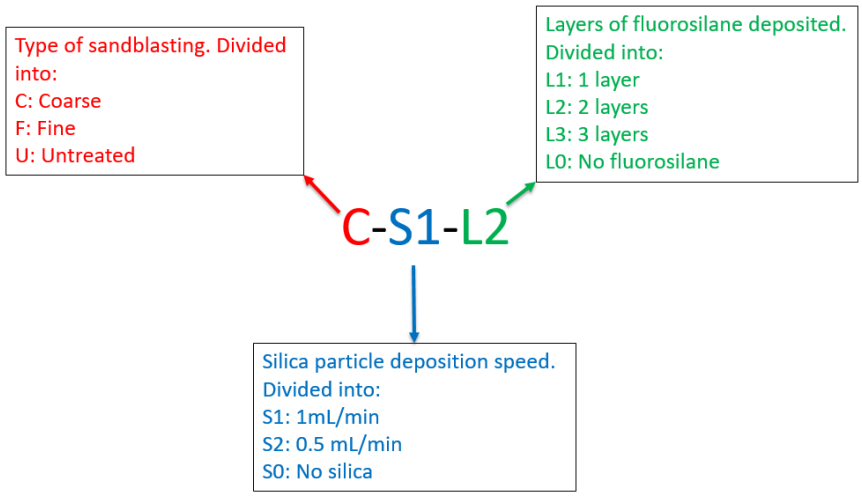

Figure 3.5: An explanation of the naming system used for the samples. The name C-S1-L2 is used as an example. The first part (here: C) signifies which type of sand the substrate was sandblasted with. The second part (S1) shows the deposition speed at which the silica particle sol were spray coated. The third part (L2) shows the number of fluorosilane sol layers spray coated onto each substrate.

Table 3.3: A table giving an overview of all samples prepared. The columns are divided into the main parameters which were modified per sample.

Sample name	Sandblasting type	Silica particle deposition speed [mL/min]	Number of fluorosilane layers deposited
F-S1-L1	Fine	1.0	1
F-S1-L2	Fine	1.0	2
F-S1-L3	Fine	1.0	3
F-S1-L4	Fine	1.0	4
F-S1-L0	Fine	1.0	0
F-S2-L3	Fine	0.5	3
F-S0-L2	Fine	0	2
F-S0-L0	Fine	0	0
C-S1-L1	Coarse	1.0	1
C-S1-L2	Coarse	1.0	2
C-S1-L3	Coarse	1.0	3
C-S0-L2	Coarse	0	2
C-S0-L0	Coarse	0	0
U-S0-L2	Untreated	0	2
U-S0-L0	Untreated	0	0

3.9 Weight gain

To investigate the amount of coating applied to the substrates, and the amount of solvents evaporated during heat treatment, some samples were weighed before and after these steps. The scale used was a Sartorius ME235P analytical balance scale. A picture of the scale is shown in figure 3.6.

Figure 3.6: The Sartorius ME235P analytical balance scale used for weight measurements.

3.10 Micro- and nanostructure characterization

To image the micro- and nanostructure of the substrate surfaces, a Zeiss Supra 55 VP Low Voltage Field Emission Scanning Electron Microscopy was used, hereafter referred to as the SEM. Samples were imaged using the secondary electron detector. The parameters used were mainly working distances of 8.5 mm and 6.5 mm, an aperture of 30 µm, and an acceleration voltage of 5 kV, unless otherwise noted. Backscattered electron mode was also attempted. The purpose was to be able to separate different phases on the surface. The parameters used here were an aperture of 60 µm, a working distance of 10.2 mm and 5 kV acceleration voltage.

The size of the deposited silica nanoparticles was estimated using SEM images, along with ImageJ image analysis software. The apparent size of the particles were compared to the length scale at that magnification as displayed by the SEM software.

To investigate the interface structure, the cross section of sample C-S1-L2 was imaged. The sample was positioned vertically in 15 mL PolyFast thermoplastic powder in a Struers casting machine. The sample was cast at 180 °C for 5 min,

hardening the PolyFast powder around the sample. The cast was then ground down approximately 5 mm to expose the sample surface and coating. The grinding was performed using a Struers grinding machine and Silicon Carbide grinding paper, types 80, 220 and 320. The surface of the cast was polished using a Struers polishing machine. It was polished by using polishing plates and diamond slurry, with three runs of 3 min each. The sample was cleaned with ethanol and water between each polishing step. After polishing, the sample was imaged in the SEM. Later, a carbon coater was used to coat the surface of the cross section with carbon. The purpose of the carbon coating was to avoid charge build-up when imaged in the SEM. Finally, the cross section was imaged in the SEM a second time.

3.11 Characterization of hydrophobicity

To characterize the hydrophobicity of the finished substrates, a Drop Shape Analyzer from KRÜSS GmbH was used, known as DSA100 and shown in figure 3.7. The hydrophobicity of the substrates was characterized through contact angle and contact angle hysteresis measurements.

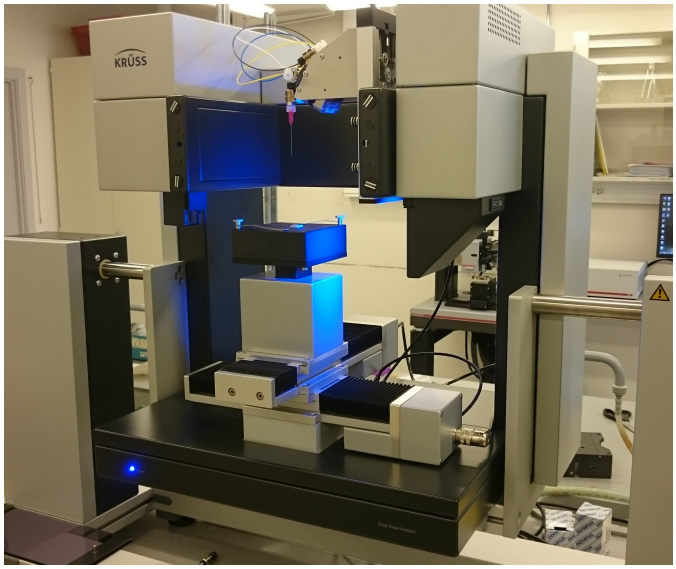

Figure 3.7: The Drop Shape Analyzer DSA100 used for hydrophobicity characterization.

3.11.1 Contact angle

The contact angles (CA) of water on the substrates were measured. To accomplish this, water droplets were deposited onto the substrates. The alignment of the

substrate and the deposition of water droplets was controlled by KRÜSS Advance software running on a separate computer. The deposition process could be done manually through the software, or it could be automated. The deposition itself was done by a thin needle connected to a syringe controlled by the Advance software. After deposition, a high speed camera was used to capture still frames of the droplet on the surface. These frames were analysed by the software using an algorithm based on the Young-Laplace equation. The software attempted to find the contact baseline between droplet and surface, and calculated the droplet CA. In practice, the contact baseline often had to be set manually, and the CA re-analysed.Additional information was also recorded, such as the temperature recorded by a temperature sensor, and time of measurement.

The size of the deposited droplets were set to be 8 µL of DI water. The Advance drop shape analyzer software also made a volume estimate of deposited droplets based on measurements taken by the camera. The volume estimation was based on a size comparison with a known size, and the droplet depositing needle was used. The needle was measured with a micrometer, and its diameter entered into the software. The DSA100 used camera settings controlled by the KRÜSS Advance software. All measurements were done using the following settings: 40 brightness, 85 zoom, 51 focus and 20 FPS. The camera itself was physically tilted 2° in relation to the plane of the substrate, to make the baseline more accurate.

The DSA100 allowed for a large degree of automation in its operation, allowing the measurements to be taken with very precise timing. The measurements done has taken full advantage of its potential for accuracy, ensuring the measurements were done at the exact same time after each droplet was deposited. Eleven measurements were done in the first six seconds after the droplet was deposited, with one measurement per 0.5 s.

The CA measurements were repeated on three different areas on each substrate, giving a total of 33 measurements per substrate. To avoid any edge effects, the droplets were deposited some distance away from the edges of the substrate. The droplets were also not deposited on areas which were already measured, to avoid any potential effects the droplets might have had on the surface. Because of the droplet volume and substrate size, this allowed for three measurement areas per substrate, as can be seen in figure 3.8.

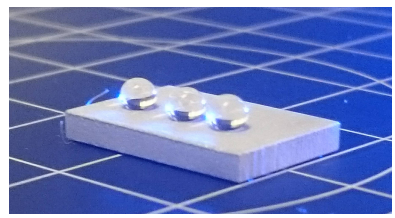

Figure 3.8: Three sessile droplets deposited on a sample substrate. The droplets are deposited in the typical positions where measurements were made on the substrates.

3.11.2 Contact angle hysteresis

An external tilting table connected to the DSA100 allowed the samples to be tilted a maximum of 90°. An example of the tilting function in use is shown in figure 3.9. The tilting function was used to determine the roll off angle (ROA) and contact angle hysteresis (CAH) for the coated substrates. An experimental procedure was used wherein a 8 µL droplet was deposited onto the substrates, and after a few seconds the tilting table was used to start tilting the DSA100. For the initial measurements, the table was tilted 1 °/s, and each second a still frame measurement was recorded by the camera. If the droplet rolled off before the table was tilted 90°, then a more careful measurement was made. To increase the accuracy of determining the angle at which the droplet rolled off, i.e. the ROA, new droplets were deposited and the table tilted by 0.5 °/s, with 2 measurements per second. At the frame that the droplet started moving, or complete roll off occurred, the tilting angle was recorded as the ROA. The previous frame, where roll off had yet to occur, was used to find the CAH. The angle of each side of the droplet to the baseline was found using a tangent fitting algorithm in the software. The angle difference, i.e. the CAH, was recorded manually. The samples being characterized were fastened while tilting with either two clamps or adhesive tape.

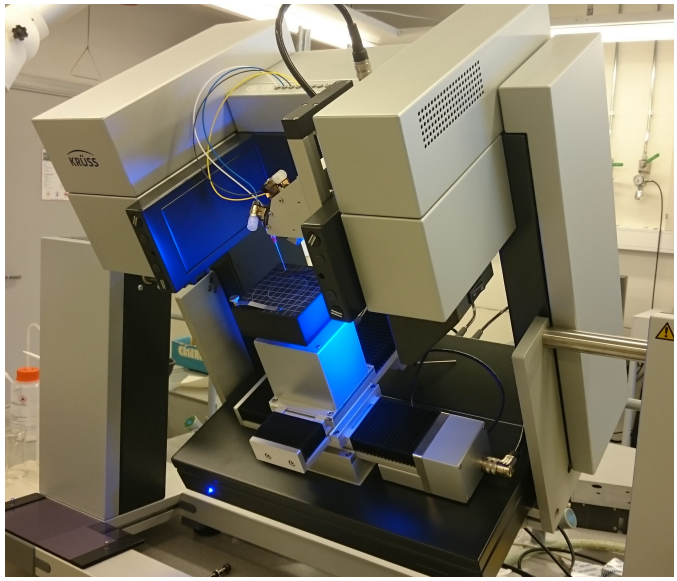

Figure 3.9: A picture of the DSA100 being tilted 30° by the external tilting table.

Typically, 2 measurements of the contact angle hysteresis were made per sample. Any more measurements could not be made without measuring on areas of the substrate that had already been measured upon, and to avoid touching the edges.

3.11.3 Environmental behaviour

An environmental chamber, the TC40, and a humidity chamber, the HC10, were used to investigate the environmental behaviour of the substrates. The HC10 was connected to the TC40, which itself was connected to the DSA100. The TC40 was an enclosed, temperature-controlled environmental chamber. The temperature in the chamber was controlled manually by using two devices: a water/ethylene glycol cooling system, controlled externally by a Julabo F12-MA Circulator system, and a Peltier element, allowing for fine-tuning of the temperature. The samples to be tested were placed on a platform in the chamber with good heat-conductance, which the Peltier element was directly connected to. The HC10 as it was installed onto the TC40, controlled the humidity levels inside the TC40. The HC10 was connected to a Silver Line air compressor, which in combination with a container of distilled water was used to control the humidity. The air compressor was set to deliver a constant 1 bar of pressure. A thermal hood could be inserted into the TC40, which improved control over temperature, but reduced control over humidity.

A temperature sensor connected to the DSA100 was inserted into the chamber, enabling the software to measure the temperature inside the chamber. The temperature sensor was taped down to constantly be in contact with the sample platform, in order to most accurately measure the substrate temperature. A second temperature sensor was connected to the HC10. A small opening in the top of the environmental chamber allowed for the droplet depositing needle to enter the chamber.

Contact angle reduction with reducing temperature

The effect of temperature on the static contact angle was examined. In these tests, samples were gradually cooled from 22 °C to 5 °C, while measuring the development in CA. To accomplish this, a sample was placed in the environmental chamber holding 22 °C. An 8 µL droplet was then deposited on the sample. The thermostat temperature connected to the Peltier element was manually lowered at a rate of −1 °C/min. A measurement was taken in the KRÜSS Advance software each minute during cooling. This process was continued until the measured temperature inside the chamber was approximately 5 °C. The thermal hood was utilized in these experiments to improve temperature control. But as a result the humidity levels fluctuated in the range of 60 - 70%. The water/ethylene glycol cooling system was kept at 15 °C.

Contact angle reduction with evaporation

The change in static contact angle over time was also investigated. The purpose was to examine the effect that evaporation had on the CA of a droplet. An 8 µL droplet was deposited on a sample, and its CA measured every minute for 30 minutes. The sample was kept at 22 °C, and the humidity was kept in the range of 60 - 65%.

3.12 Characterization of anti-icing properties

To characterize the anti-icing properties of the substrates, the DSA100 was used. Only the environmental chamber TC40 was connected to the DSA100 for these experiments. The HC10 humidity chamber could not be used below 5 °C. Therefore, humidity levels could not be precisely controlled during the anti-icing characterization. The TC40 without the HC10 installed is shown in figure 3.10. The water/ethylene glycol cooling system was kept in the range of −2 °C to 3 °C. The thermal hood was utilized during these experiments to improve temperature control.

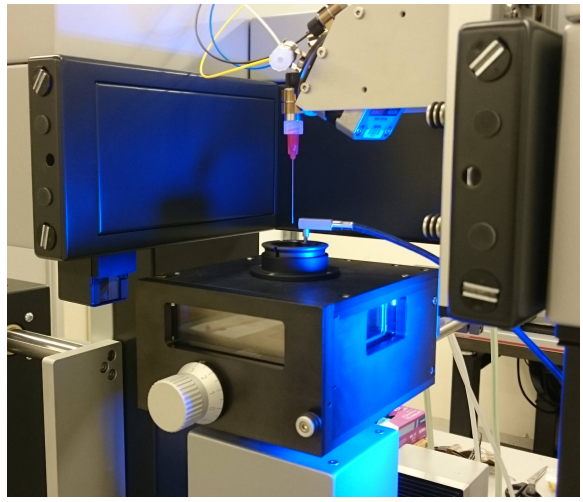

Figure 3.10: An environmental chamber, the TC40, installed in the DSA100.

Three anti-icing properties were tested for. These include the nucleation temperature, the delay of ice formation and cyclic icing behaviour. The experimental procedures are largely based on [1] with modifications.

3.12.1 Nucleation temperature

For the nucleation temperature measurements, a substrate was placed in the environmental chamber at ambient conditions. The temperature in the chamber was then gradually lowered to 5 °C. This was done by lowering the thermostat temperature for the Peltier element to 3 °C, because of a discrepancy between the temperature set and the temperature that was measured. It was kept at 5 °C for 10 min to ensure the sample was at thermal equilibrium. Then, an 8 µL sessile droplet was deposited onto the sample surface. The thermostat temperature connected to the Peltier element was manually lowered at a rate of −1 °C/min. For many samples, a measurement was made in the KRÜSS Advance software each minute during cooling. The thermostat temperature was lowered at a constant rate

until the sessile droplet froze. The freezing process was recorded by the software, and the temperature was recorded by the temperature sensor each frame. This allowed for precise determination of the freezing temperature.

For some samples, a three-droplet test was performed. This was done to investigate the homogeneity of the surface and ascertain the uncertainty of the nucleation temperature measurements. Three droplets were deposited on separate areas of the sample before cooling began, similar to figure 3.8. The temperature at which each droplet froze was recorded during cooling.

3.12.2 Delay of ice formation

To test the delay of ice formation, the environmental chamber containing a sample was first lowered to $-10\,^{\circ}\mathrm{C}$. The temperature was maintained for at least 10 min to ensure thermal equilibrium. The deposition needle was then lowered into the chamber, and an 8 µL sessile droplet was deposited onto the substrate. When the droplet came into contact with the surface, a timer was started. The chamber temperature was maintained at $-10\,^{\circ}\mathrm{C}$ until the droplet froze. The timer was then stopped, and the time recorded was found as the delay of freezing. For samples that showed some delay of ice formation, a measurement was made in the Advance software every 5 min. For some samples, three droplets were deposited on different areas, and the time was taken before each droplet froze.

3.12.3 Cyclic icing behaviour

Finally, the cyclic icing behaviour of the samples were investigated. First, a procedure similar to the nucleation temperature tests were performed. An 8 µL sessile droplet was deposited at $5\,^{\circ}\mathrm{C}$ on a sample and the chamber temperature was lowered at $-1\,^{\circ}\mathrm{C}$/min until freezing. The contact angle of the droplet was measured every minute during cooling until it froze. The droplet freezing temperature was recorded as normal. After freezing, the Peltier thermostat was increased in temperature by $2\,^{\circ}\mathrm{C}$/min, until it reached $5\,^{\circ}\mathrm{C}$ again. The chamber was kept at $5\,^{\circ}\mathrm{C}$ for approximately 10 min. Then, the same process was repeated two or three more times, with the temperature of freezing being recorded each time.

To ascertain the uncertainty in the ice cycling measurements, and investigate the homogeneity of the surface, the ice cycling tests were performed using three droplets simultaneously on certain samples. Three droplets were deposited on separate areas of the sample at $5\,^{\circ}\mathrm{C}$, similar to figure 3.8. Then, the temperature was lowered by $-1\,^{\circ}\mathrm{C}$/min until all three droplets froze. The freezing temperature was recorded individually for each droplet. The ice cycling process was repeated two or three more times, similar to the single droplet method. The camera zoom was set to 40 for these experiments to allow viewing all three droplets simultaneously.

3.12.4 Coating durability

The coating durability was tested by measuring contact angles, contact angle hysteresis and nucleation temperature on sample C-S1-L1, after it had been subject to all three types of icing characterization. In total, sample C-S1-L1 had been subject to one nucleation temperature test, one delay of icing test, one single droplet ice cycling test, as well as one three-droplet ice cycling test. The contact angles and hysteresis were measured through the same procedure as those detailed in section 3.11. The droplets were deposited on approximately the same positions as the ones used for the three-droplet ice cycling test, though with some variance likely to occur.

Chapter 4

Results

4.1 Substrate characterization

4.1.1 Effects of sandblasting

Substrates sandblasted with coarse and fine sand became visibly distinct, not just compared to an untreated substrate but also to each other. The difference in appearance is shown in figure 4.1.

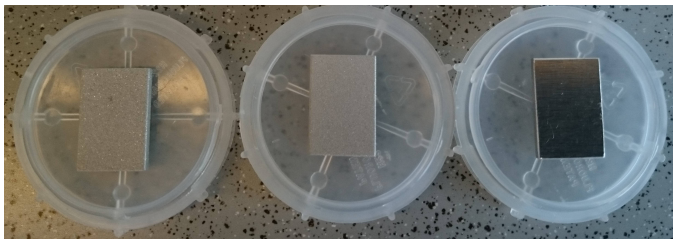

Figure 4.1: A picture showing the difference in appearance between the different sandblasting types. From left to right are substrates sandblasted with coarse sand, fine sand and no sandblasting respectively.

4.1.2 Roughness measurements of sandblasted substrates

The average roughness of the substrates sandblasted with fine particles was found to be $2.83 \pm 0.15\,\mu m$.

The roughness of the substrates sandblasted with coarse sand was also measured. However, the roughness proved to be outside the measuring limitations of the

profilometer. The only data acquired from these measurements was that the average roughness was above 7 µm.

4.1.3 Weight gain

Table 4.1 shows the weight changes measured for the samples before and after coating with fluorosilane, in addition to after heat treatment.

Table 4.1: An overview of the weight changes of several samples before and after coating with fluorosilane and after heat treatment. The difference in weight after the fluorosilane coating step and after the heat treatment are shown. Finally, the total differences are shown in the rightmost column. All values may have an error of ±0.02 mg from the scale.

	Sample weight [mg]		
Sample name	Weight difference after coating	Weight difference after heat treatment	Total difference
C-S1-L1	0.22	-0.41	-0.19
C-S1-L2	0.43	-0.32	0.11
C-S1-L3	1.12	-0.96	0.16
C-S0-L2	1.38	-1.09	0.29
F-S2-L3	1.08	-0.82	0.26

4.1.4 Micro- and nanostructure characterization

Effects of sandblasting

Figure 4.2 shows a comparison of the resulting microroughness of substrates sandblasted with either fine or coarse sand.

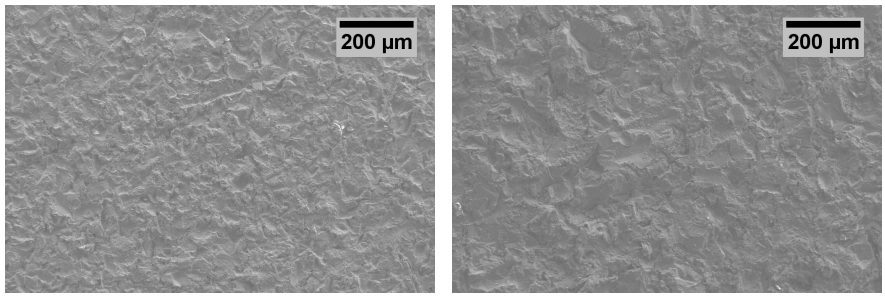

(a) SEM image of sample F-S0-L0. **(b)** SEM image of sample C-S0-L0.

Figure 4.2: A comparison of SEM images taken of samples F-S0-L0 and C-S0-L0.

Effects of silica nanoparticle deposition

Figure 4.3 shows SEM images taken from sample F-S1-L0, i.e. a sample which was sandblasted with fine sand and coated with silica particles, but not with fluorosilane. Another SEM image taken of sample F-S1-L0 is shown in figure 4.4. As can be seen from the figures, the deposited density of silica nanoparticles has some variability. Certain areas can be seen to only have a monolayer of particles, or an even less dense layer, where the aluminium surface is visible beneath. This can be seen highlighted in the upper right of figure 4.3, or the upper part of figure 4.4. Here, features of the sandblasted aluminium surface are exposed with only a few particles deposited on top. Other areas, such as the one highlighted in the upper left of figure 4.3, had a much greater density of particles. Here, a relatively thick layer of closely packed spheres have formed. Fracture lines run through and split the dense particle deposition.

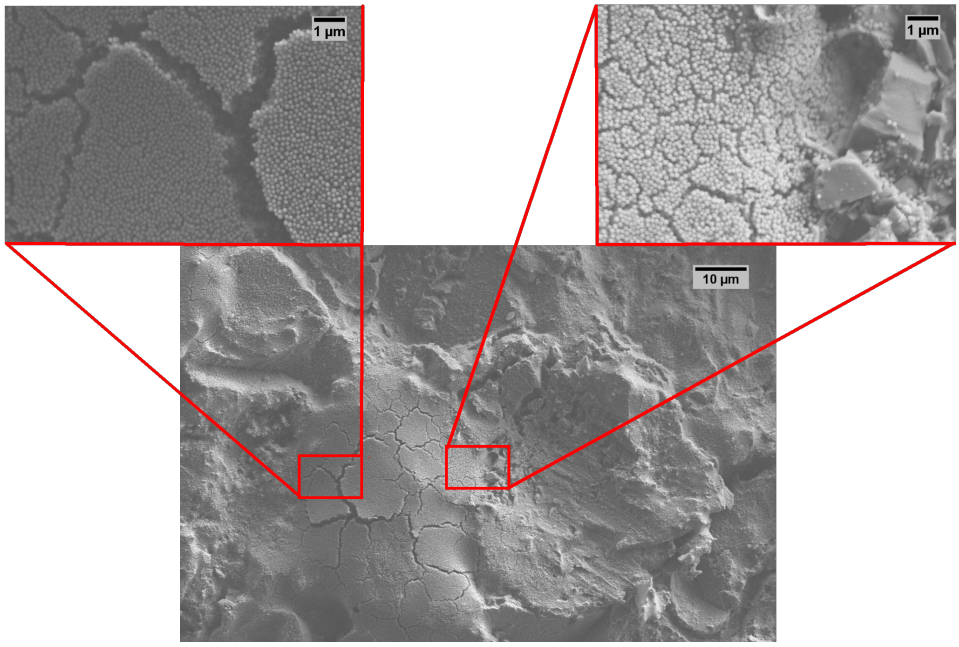

Figure 4.3: SEM images taken of sample F-S1-L0. On the bottom is a larger overlook of the distribution of silica particles on the surface. The red rectangles show two areas of high magnification, these are shown on the top left and right of the figure.

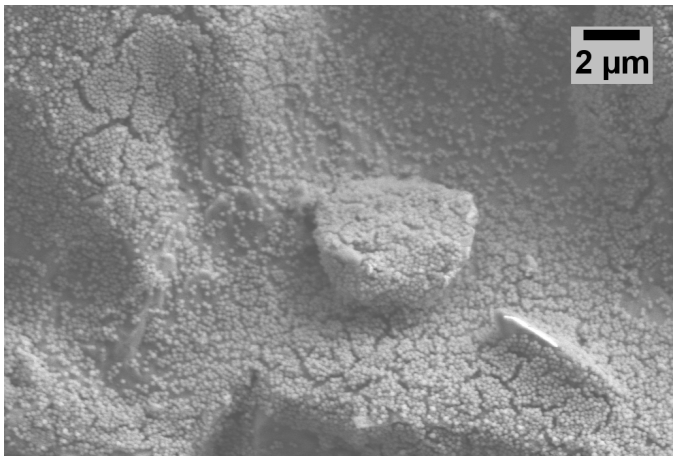

Figure 4.4: SEM image taken of silica nanoparticles deposited on sample F-S1-L0.

Effects of fluorosilane sol-gel deposition

Figure 4.5 shows SEM images comparing the final surface of samples F-S1-L4 and C-S1-L3. It was not possible to detect the fluorosilane coating directly through SEM. Backscattered electron mode was attempted, but did not yield any usable results.

Figure 4.6 and 4.7 shows the silica particle distribution on the surface of sample C-S1-L3. On areas without charge build-up, the particle coverage was similar to the one seen in 4.4 for sample F-S1-L0. Generally, a single layer of particles were spread across the surface, with minimal stacking.

Figure 4.8 shows SEM images of the surface of sample F-S2-L3, i.e. a coated sample with reduced silica particle deposition. Of particular note is the lower density of silica particles deposited on the surface.

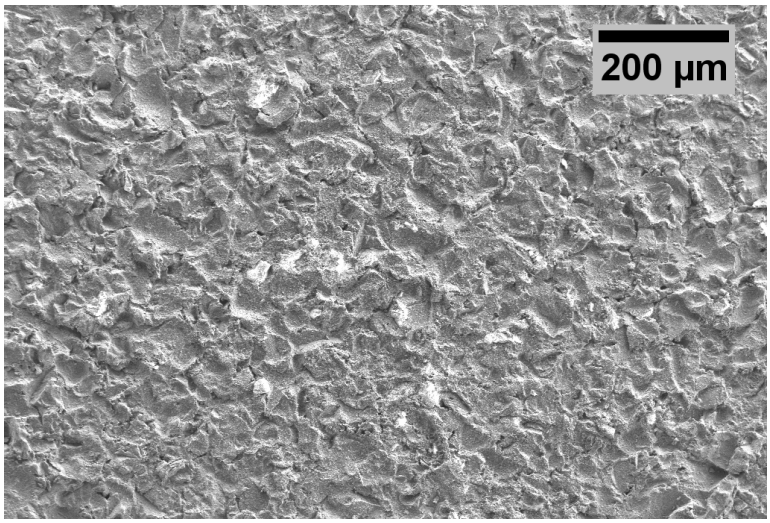

(a) SEM image of sample F-S1-L4.

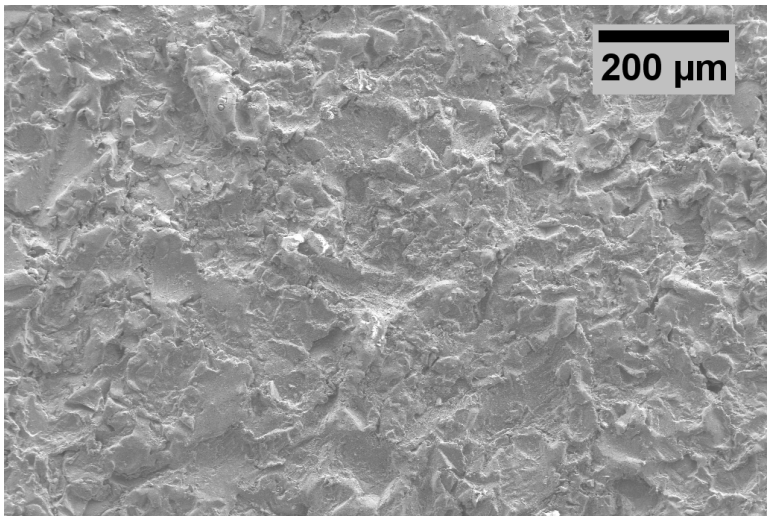

(b) SEM image of sample C-S1-L3.

Figure 4.5: A comparison of the microstructure on samples F-S1-L4 and C-S1-L3.

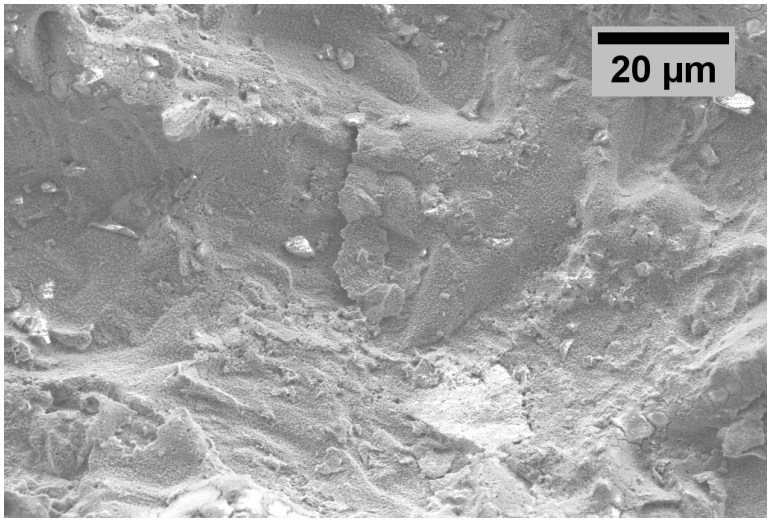

Figure 4.6: SEM image taken of sample C-S1-L3, showing the microstructure covered with silica particles.

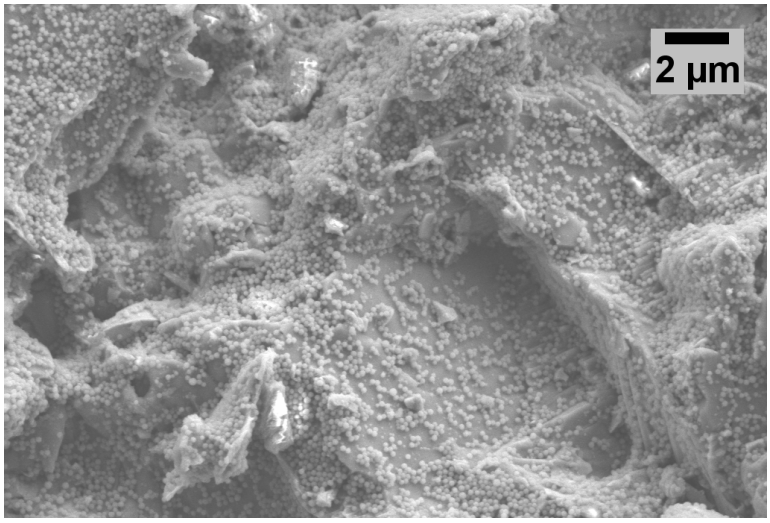

Figure 4.7: SEM image taken of sample C-S1-L3, showing a typical distribution of silica particles on the surface.

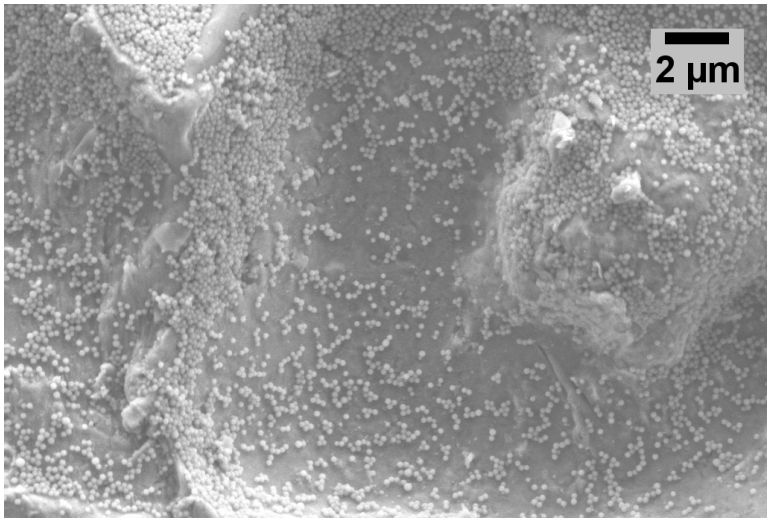

(a)

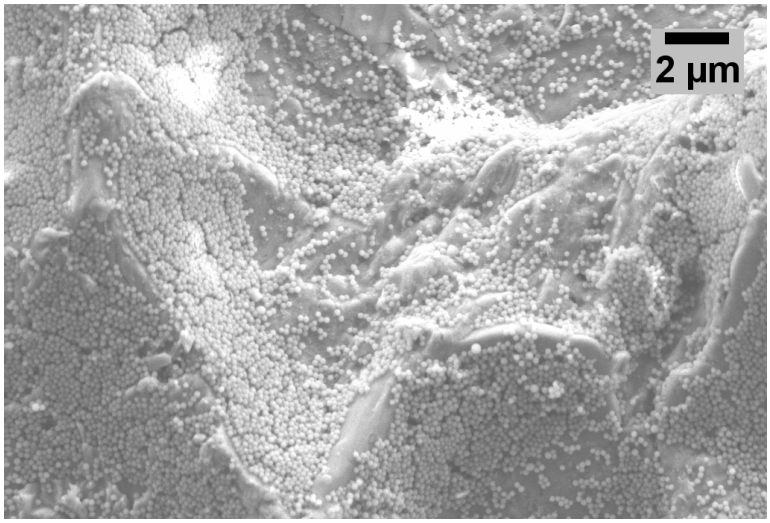

(b)

Figure 4.8: SEM images of sample F-S2-L3. The images show the silica particle coverage at two areas of the surface. **(a)** shows a more sparsely covered area, while **(b)** shows an area with larger particle density.

Nanoparticle size analysis

The size of the deposited nanoparticles were estimated using the SEM image shown in figure 4.9. The length of 20 particles were measured and compared with the scale bar. The estimated particle size was found to be 186 ± 12 nm.

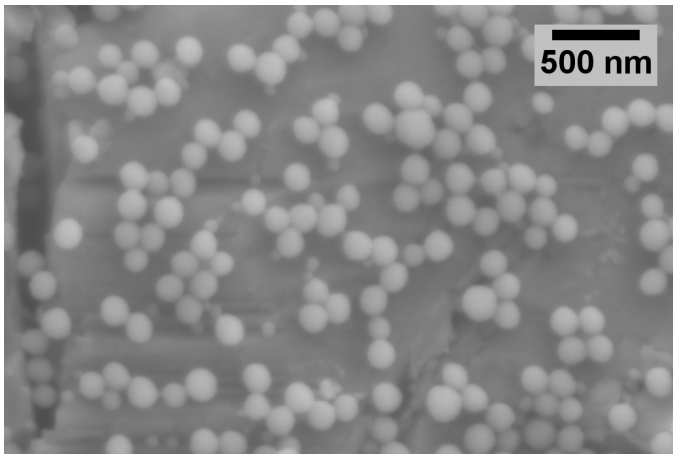

Figure 4.9: A SEM image of sample C-S1-L3, showing silica nanoparticles.

Cross section analysis

A picture of the cross section of sample C-S1-L2 as it was molded in thermoplastic is shown in figure 4.10.

Figure 4.10: A picture of sample C-S1-L2 that has been molded into thermoplastic, then ground and polished to expose its cross section.

An overview of the cross section profile for sample C-S1-L2 can be seen in figure 4.11. The microstructure roughness induced by the coarse sandblasting is clearly visible.

Figure 4.11: A SEM image showing the cross section profile of sample C-S1-L2 coated with carbon. The bottom area is the aluminium sample, while the top area is the thermoplastic mold.

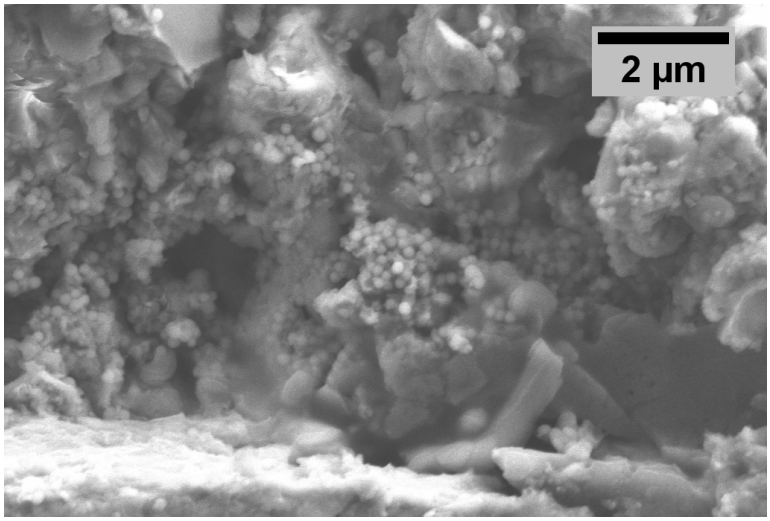

Figure 4.12: A SEM image showing the cross section of sample C-S1-L2 coated with carbon. The aluminium sample is on the bottom.

Figure 4.12 shows a closer look at the surface cross section after coating with carbon. Silica nanoparticles are visible as they are spread across the microstructure.

4.2 Characterization of hydrophobicity

4.2.1 Contact angle measurements

An overview of the static contact angles found for each substrate can be found in table 4.2. The values are additionally illustrated in a chart in figure 4.14. The volume of the droplets deposited were estimated by the Advance software to be $8 \pm 2\,\mu L$, while the droplet depositing needle was 0.513 mm in diameter. An example of a contact angle measurement is shown in figure 4.13.

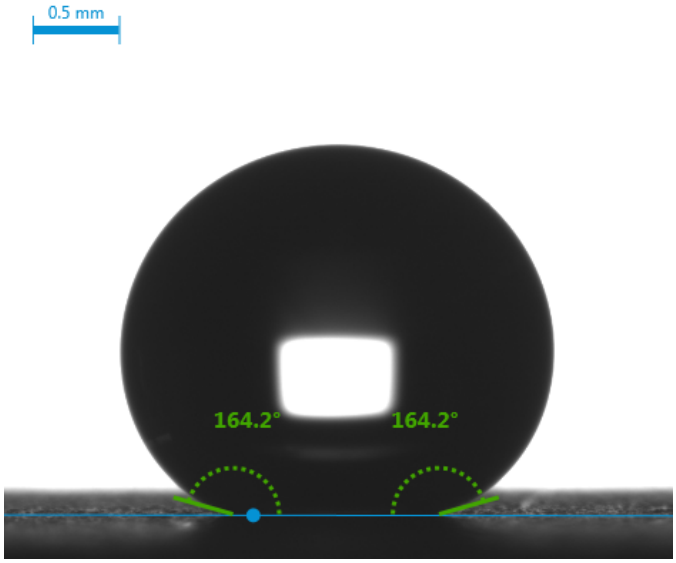

Figure 4.13: A picture of a contact angle measurement. The sample being measured upon is F-S1-L4, at area 2.

Table 4.2: A table of the static contact angles found through the contact angle measurements. The results are divided into the 3 areas that were tested on each sample, with the average contact angle per sample shown in the rightmost column. The variance per area is the standard deviation of the 11 measurements per droplet done for that area. The results in the "Average" column are the mean contact angle based on the three averages from the three areas. The variance is the standard deviation of the result averages from the three areas.

	Contact angle [°]			
Sample name	Area 1	Area 2	Area 3	Average
F-S1-L1	163.0 ± 0.1	158.8 ± 0.3	162.0 ± 0.2	161.2 ± 2.2
F-S1-L2	159.5 ± 0.3	163.5 ± 0.3	158.0 ± 0.5	160.3 ± 2.9
F-S1-L3	159.9 ± 0.3	160.2 ± 0.2	159.0 ± 0.6	159.7 ± 0.6
F-S1-L4	162.5 ± 0.3	164.2 ± 0.3	163.2 ± 0.2	163.3 ± 0.8
F-S2-L3	163.7 ± 0.4	163.4 ± 0.3	152.7 ± 0.2	159.9 ± 6.3
F-S0-L2	159.3 ± 0.3	156.9 ± 0.1	151.5 ± 0.2	155.9 ± 4.0
F-S0-L0	60.8 ± 0.4	56.5 ± 0.2	49.3 ± 0.1	56 ± 6
C-S1-L1	165.3 ± 1.7	164.7 ± 0.5	167.1 ± 1.3	165.7 ± 1.3
C-S1-L2	162.4 ± 0.2	163.1 ± 0.5	163.1 ± 1.5	162.8 ± 0.4
C-S1-L3	161.7 ± 0.6	161.6 ± 0.6	161.7 ± 0.4	161.7 ± 0.1
C-S0-L2	156.5 ± 0.1	157.9 ± 0.1	154.8 ± 0.1	156.4 ± 1.6
C-S0-L0	56.9 ± 0.2	62.1 ± 0.2	52.2 ± 0.2	57 ± 5
U-S0-L2	95.9 ± 1.7	107.8 ± 1.0	92.3 ± 2.4	99 ± 8
U-S0-L0	55.6 ± 0.1	66.8 ± 0.2	62.1 ± 0.2	62 ± 6

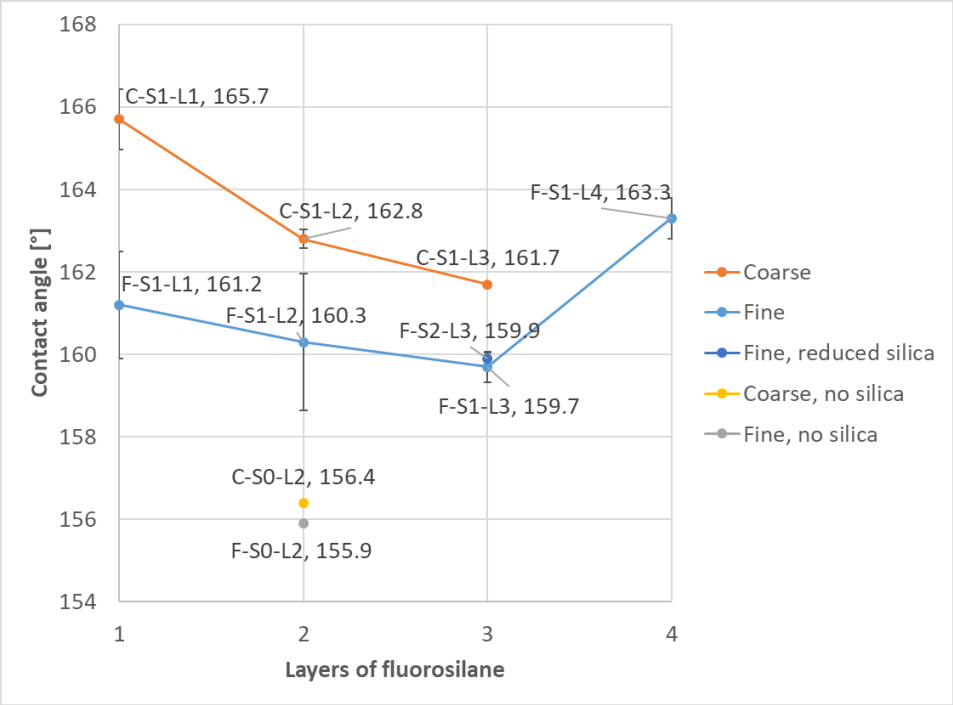

Figure 4.14: A chart showing the average static contact angles for certain samples, which are summarized in table 4.2. The error bars are the standard error of the 3 average results for that sample. The error bars for samples F-S2-L3, C-S0-L2 and F-S0-L2 are not included to retain clarity.

4.2.2 Contact angle hysteresis measurements

Table 4.3 shows an overview of the measured Roll Off Angle (ROA) and Contact Angle Hysteresis (CAH) for the different samples. An example of the ROA and CAH measurements can be seen in figure 4.15a. The CAH could not be found for samples that had a greater ROA than 90°, as the CAH should be measured the frame before roll off. However, it was observed that the contact angle difference for such samples were greater than 50° when tilted 90°. An example is shown in figure 4.15b.

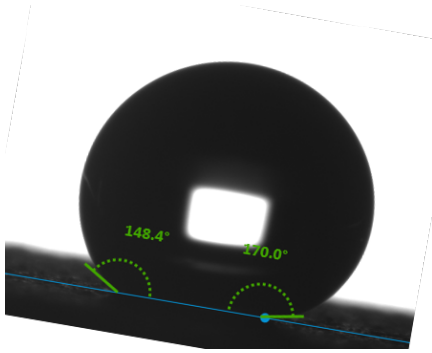

(a) CAH measurement on sample C-S1-L1. In this case a droplet exhibited a 21.6° CAH at a 9.71° tilt, which was the last frame before roll off.

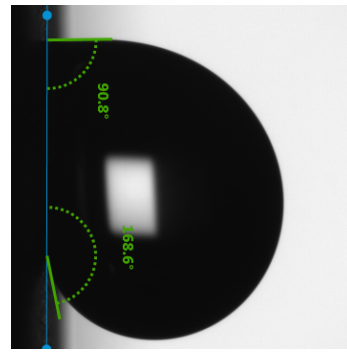

(b) CAH measurement on sample F-S1-L4. The DSA100 is tilted 90°. A large deformation of the droplet profile can be seen due to the strong contact line pinning working against gravity.

Figure 4.15: Examples of CAH measurements.

Table 4.3: A table showing the average Roll Off Angle (ROA) and Contact Angle Hysteresis (CAH) for the different samples. The ROA is given as $> 90°$ if the droplet did not roll of during tilting. The variance shown for each value is the standard deviation of each group of measurements.

Sample name	Roll off angle [°]	Contact Angle Hysteresis [°]
F-S1-L1	$> 90°$	-
F-S1-L2	$> 90°$	-
F-S1-L3	$> 90°$	-
F-S1-L4	$> 90°$	-
F-S2-L3	$> 90°$	-
F-S0-L2	$> 90°$	-
F-S0-L0	$> 90°$	-
C-S1-L1	9.2 ± 0.6	22.8 ± 1.6
C-S1-L2	12.3 ± 1.8	45.6 ± 10.8
C-S1-L3	13.3 ± 7.3	33.2 ± 10.5
C-S0-L2	$> 90°$	-
C-S0-L0	$> 90°$	-
U-S0-L2	$> 90°$	-
U-S0-L0	$> 90°$	-

4.2.3 Environmental behaviour

Contact angle reduction with reducing temperature

The contact angle development as the temperature was lowered from 22 °C to 5 °C is shown in figure 4.16 for two samples.

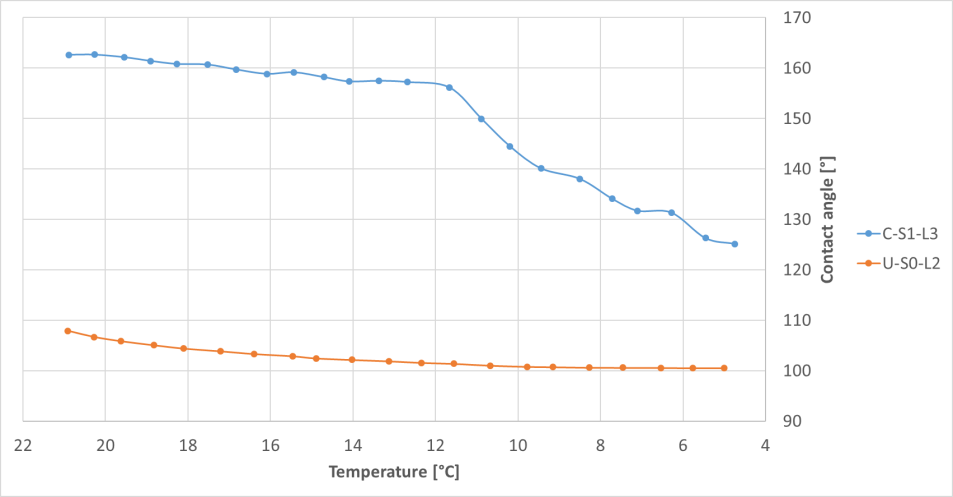

Figure 4.16: A chart showing the contact angle development for a droplet deposited on samples C-S1-L3 and U-S0-L2.

It should be noted that a certain amount of evaporation occurred for the droplets as they were cooled down from 22 °C to 5 °C. The change in estimated volume per degree of cooling is shown in figure 4.17.

Contact angle reduction with evaporation

Figure 4.18 shows how the contact angle changed for a droplet deposited on C-S1-L3 during the evaporation test.

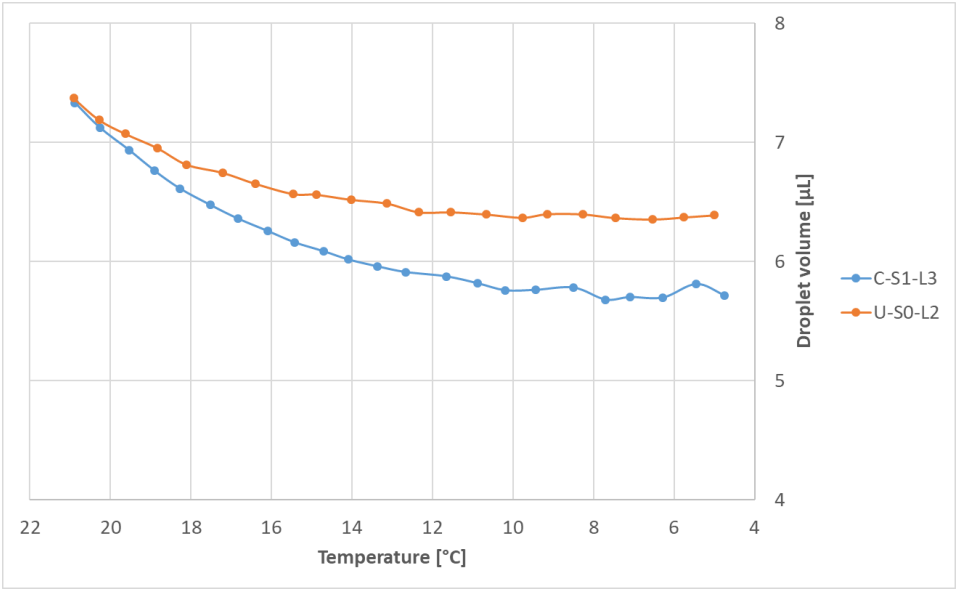

Figure 4.17: A chart showing how the volume of the droplets deposited on samples C-S1-L3 and U-S0-L2 varied during cooling.

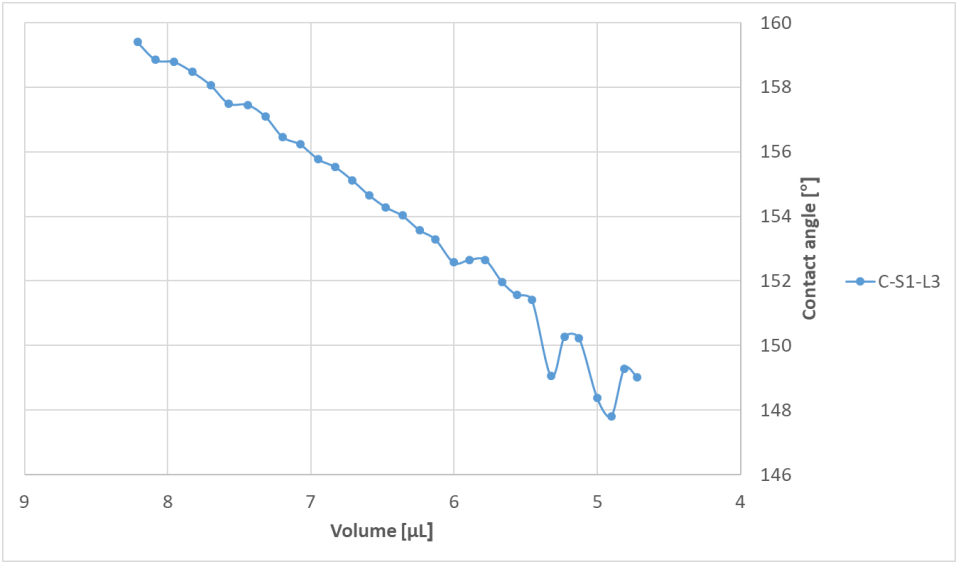

Figure 4.18: A chart of the contact angle change for a droplet deposited on C-S1-L3 as the droplet evaporated.

4.3 Characterization of anti-icing properties

The results of each anti-icing characterization method are summarized in the following sections.

4.3.1 Nucleation temperature

The nucleation temperatures found during the single droplet characterization are summarized in table 4.4, while table 4.5 shows the three-droplet characterization. The temperature noted is the temperature registered by the temperature sensor at the time of nucleation, and not the temperature set by the thermostat.

Table 4.4: The temperature at which a droplet froze on each sample during the nucleation temperature characterization.

Sample name	Nucleation temperature [°C]
F-S1-L1	−8.5
F-S1-L2	−9.3
F-S1-L3	−8.7
F-S1-L4	−8.4
C-S1-L1	−9.9
C-S1-L2	−9.3
C-S1-L3	−10.2
C-S0-L0	−5.4
U-S0-L0	−3.9

Furthermore, it is important to note that the first cycle of the ice cycling tests were identical to the nucleation temperature tests. The results from the first freezing cycle for each sample were therefore included in the dataset used to find an average nucleation temperature and its standard deviation for each sample. These are shown in table 4.6. The results in table 4.6 are compared in figure 4.19.

Table 4.5: The temperature at which each of the three droplets froze on each sample during the three-droplet nucleation temperature characterization. Only two droplets could fit on F-S0-L0 and U-S0-L0 because of the large droplet contact angle on these samples.

	Nucleation temperature [°C]			
Sample name	Area 1	Area 2	Area 3	Average
C-S1-L1	−6.2	−6.5	−6.2	-6.3 ± 0.2
C-S0-L2	−9.9	−9.7	−9.7	-9.8 ± 0.1
F-S0-L0	−3.1	−3.1	-	−3.1
U-S0-L2	−9.7	−14.0	−8.4	-10.7 ± 2.9
U-S0-L0	−4.0	−3.9	-	-4.0 ± 0.1

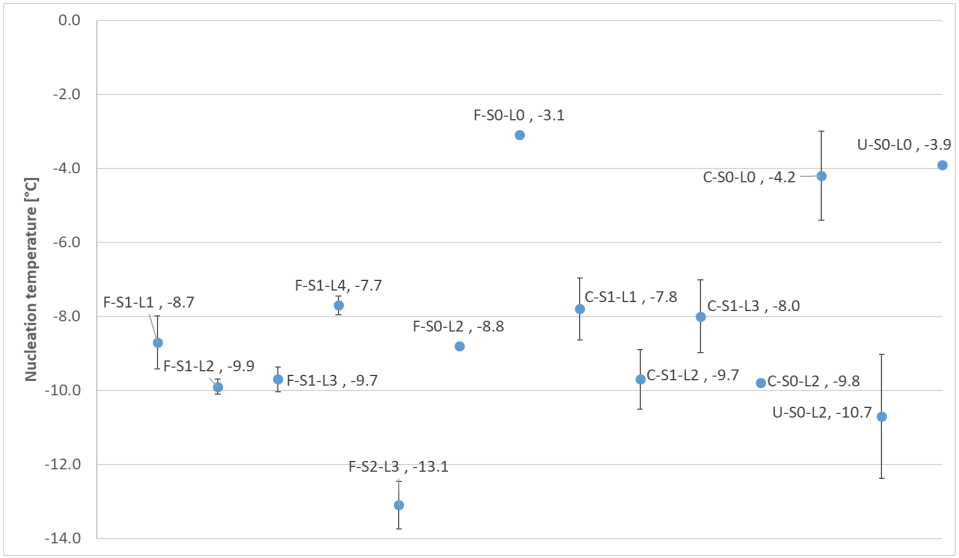

Figure 4.19: Chart of the results displayed in table 4.6. Each data point shows the average nucleation temperature for that sample. All data labels are in units of °C. The error bars are the standard error of the dataset for that sample.

Table 4.6: The average temperature at which a droplet froze on each sample during the nucleation temperature characterization, in addition to the first cycle of the cyclic icing characterization. This includes both the one-droplet and three-droplet characterization. The variance shown is the standard deviation of the entire data set for that sample.

Sample name	Average nucleation temperature [°C]
F-S1-L1	-8.7 ± 1.4
F-S1-L2	-9.9 ± 0.4
F-S1-L3	-9.7 ± 0.7
F-S1-L4	-7.7 ± 0.5
F-S2-L3	-13.1 ± 1.1
F-S0-L2	-8.8
F-S0-L0	-3.1
C-S1-L1	-7.8 ± 1.9
C-S1-L2	-9.7 ± 1.4
C-S1-L3	-8.0 ± 2.0
C-S0-L2	-9.8 ± 0.1
C-S0-L0	-4.2 ± 1.7
U-S0-L2	-10.7 ± 2.9
U-S0-L0	-3.9 ± 0.1

Freezing mechanism during nucleation temperature characterization

For the nucleation temperature characterization, the freezing process was consistently the same across every test and substrate. The freezing process is shown in figure 4.20. At a certain point during cooling, the water droplet suddenly and quickly went opaque. A freezing front appeared at the bottom of the droplet where it was in contact with the surface. The front was characterized by a darker area with less transparency. It slowly advanced up through the droplet volume and towards the top of the droplet. As the front approached the top of the droplet, some deformation of the upper profile appeared. Eventually, the freezing front reached the top of the droplet, ending in a pyramid-shaped top.

A similar freezing mechanism was observed during the three-droplet tests. Each droplet formed a frozen shell and started freezing from the substrate individually. The volume estimation of the deposited droplets performed by the Advance software showed only a small decrease during cooling. For example, for a single droplet test on sample C-S1-L2, the volume was estimated to be 7.92 µL at 5 °C, and 7.80 µL at −9.2 °C. For sample C-S1-L3, the droplet volume decreased from 9.21 µL to 8.98 µL during cooling.

Contact angle development during cooling

It was observed that the static contact angles for deposited droplets decreased as the temperature was lowered from 5 °C until freezing. This behaviour was most pronounced for coated substrates, although a small decrease was observed for an untreated substrate as well. Figure 4.21 shows this phenomenon through the contact angle development for 3 different substrates. All coarsely sandblasted substrates had higher contact angles at 5 °C and right before freezing compared to finely sandblasted substrates. All contact angle developments were not included in figure 4.21 to preserve clarity. The contact angle developments are compared in 4.7 for more substrates. The average reduction in contact angle per degree Celsius of cooling are also included.

Thermostat temperature versus actual temperature

It was found during the nucleation temperature experiments that the temperature manually set on the thermostat did not equal the temperature registered by the temperature sensor. Although the thermostat temperature was lowered by −1 °C/min, the actual temperature typically changed at a rate of −0.6 °C/min to −0.9 °C/min. For example, for a nucleation temperature experiment on sample F-S1-L3, the measured temperature dropped at a rate of -0.75 ± 0.09 °C/min. Figure 4.22 shows an overview of how the measured temperature changed for some samples compared to the set thermostat temperature.

Table 4.7: A table showing the contact angle development during cooling for some samples. The average reduction in contact angle per degree Celsius of cooling is shown in the rightmost column.

Sample name	Contact angle at 5 °C [°]	Contact angle before freezing [°]	Average CA reduction per degree Celsius of cooling [°/°C]
F-S1-L1	136.5	124.8	-1.0
F-S1-L2	124.8	114.5	-0.7
F-S1-L3	130.7	120.7	-0.8
C-S1-L1	143.7	125.4	-1.3
C-S1-L2	149.3	133.6	-1.2
C-S1-L3	140.8	131.6	-0.7
U-S0-L0	59.3	57.3	-0.2

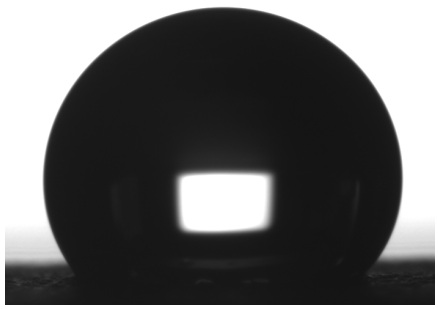

(a) One frame before freezing.

(b) The first frame after freezing.

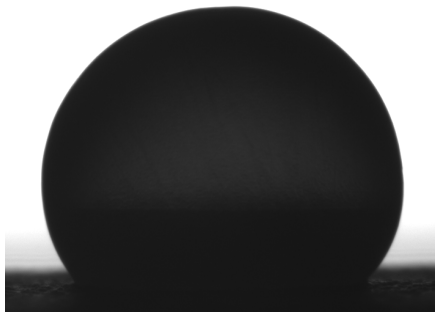

(c) 2 seconds after freezing.

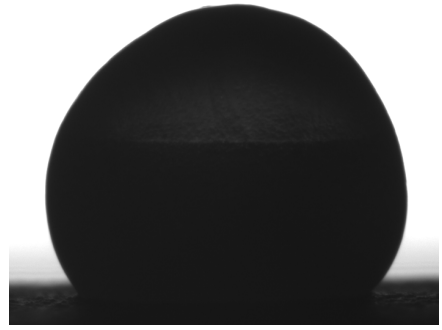

(d) 6 seconds after freezing.

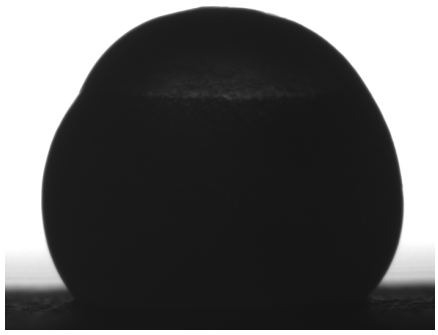

(e) 10 seconds after freezing.

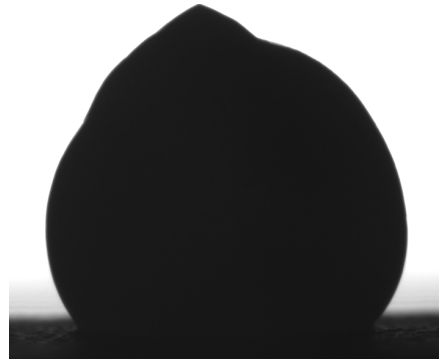

(f) 16 seconds after freezing.

Figure 4.20: Pictures showing the freezing process for a droplet deposited on sample C-S1-L3 during nucleation temperature characterization. The pictures were taken from a recording of the freezing process, and the frames before and after nucleation are shown. This droplet froze at $-10.2\,^{\circ}\mathrm{C}$.

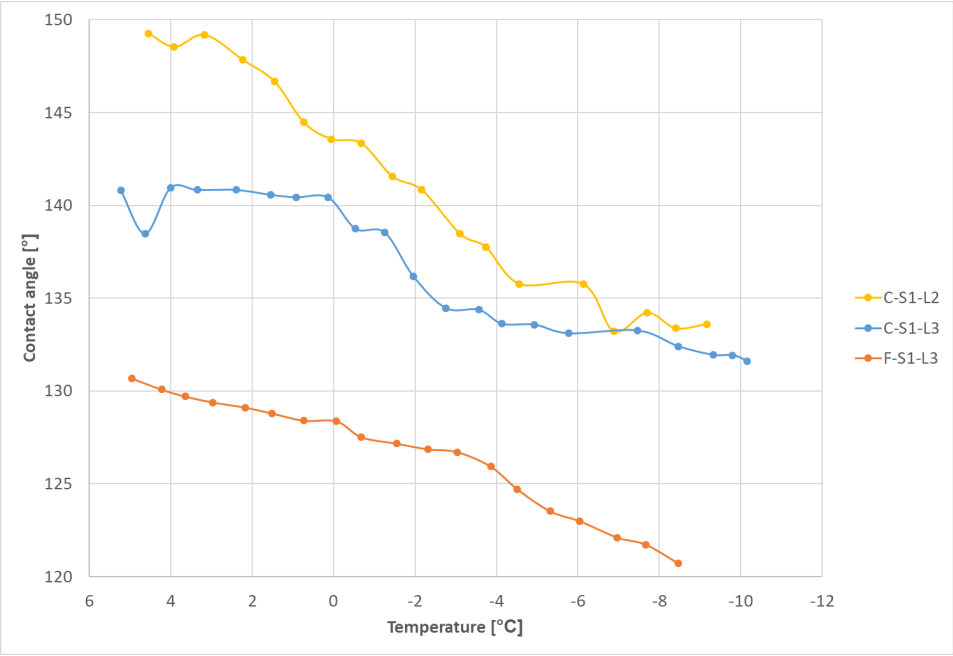

Figure 4.21: An overview of the CA development for droplets deposited during three nucleation temperature experiments on three different substrates.

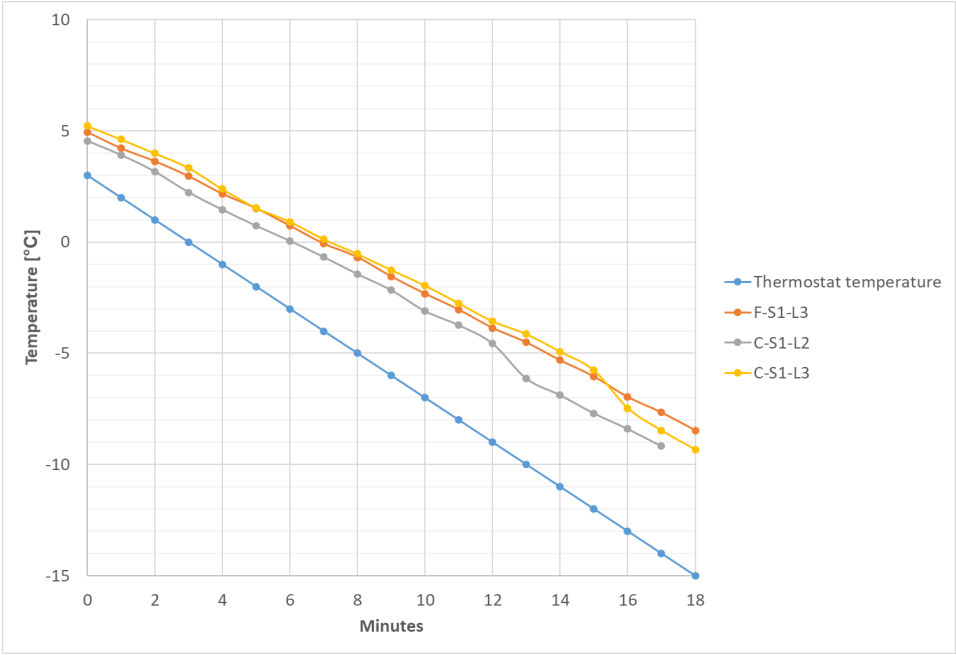

Figure 4.22: A comparison of the set thermostat temperature with the measured temperature during three instances of nucleation temperature experiments, for three different samples.

4.3.2 Delay of ice formation

Table 4.8 shows an overview of the delay of ice formation for each sample.

Table 4.8: A table showing the freezing delay for each sample that was measured. When the sessile droplet seemed to freeze immediately upon deposition, the freezing delay is marked as "None".

Sample name	Freezing delay
F-S1-L1	2 min 18 s
F-S1-L2	5 min 10 s
F-S1-L3	None
F-S1-L4	None
F-S2-L3	19 min 35 s
F-S0-L2	None
F-S0-L0	None
C-S1-L1	43 min
C-S1-L2	28 min
C-S1-L3	40 s
C-S0-L2	None
C-S0-L0	None
U-S0-L0	None

Figure 4.24 shows the development during the delay of ice formation test on substrate C-S1-L2. As can be seen from the figure, the droplet remains liquid for a certain time until it eventually nucleates. The freezing mechanism here is similar to the one observed during nucleation temperature characterization, where droplets were gradually cooled. The droplet turns opaque, and a darker freezing front slowly rises up from the surface and through the droplet. The end result is a nontransparent droplet with deformation in its upper profile, which is also visible in figure 4.20. This freezing mechanism was observed for all droplets where a certain delay before nucleation was observed. The mechanism was also observed for some droplets which froze immediately upon deposition. However, the droplets with no nucleation delay could also freeze through a second mechanism. In this case, the droplet did not turn opaque, yet started freezing from the surface. The freezing front moved slowly upwards through the droplet, forming transparent ice. The end result was a very transparent frozen droplet with no visible deformation in its upper profile. A

droplet that froze through this mechanism is shown in figure 4.23.

Figure 4.23: A picture showing a droplet frozen through the second freezing mechanism.

The contact angles at −10 °C for certain droplets that showed a delay of ice formation is summarized in table 4.9.

Table 4.9: A table showing the CA of certain droplets that showed some significant delay of ice formation.

Sample name	Contact angle [°]
F-S2-L3	116.4
C-S1-L1	129.3
C-S1-L2	129.1
C-S1-L3	133.0

Another phenomenon observed in the delay of ice formation experiments were the appearance and growth of ice crystals on the sample surfaces, away from any deposited droplet. Moisture condensed and froze, forming ice crystals on the exposed sample surfaces as they were kept at −10 °C. Typically, the density of ice crystals increased over time, and existing crystals grew in size. Figure 4.25 shows how ice crystals started to cover the surface of sample F-S1-L2. The growth of an ice crystal can also be seen in 4.24. If a water droplet was deposited onto one such ice crystal, the droplet immediately froze through the second freezing mechanism, forming a transparent frozen droplet. During droplet deposition, care was taken not to deposit droplets onto ice crystals. The immediate nucleation would not allow characterizing the anti-icing properties of the surface itself. Because the two freezing mechanisms resulted in two distinctly different droplets, it was assumed that it was possible to discern whether a droplet was deposited onto an existing nucleation point or

not. If deposition resulted in a transparent droplet, that result was not used when deciding the delay of ice formation for a sample.

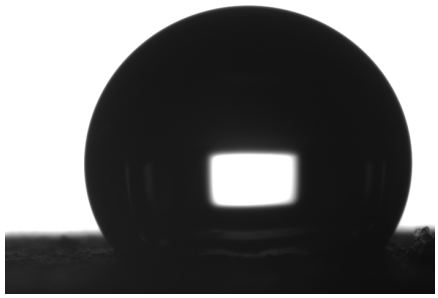

(a) 5 minutes after deposition.

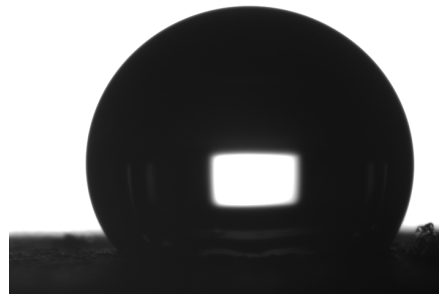

(b) 10 minutes after deposition.

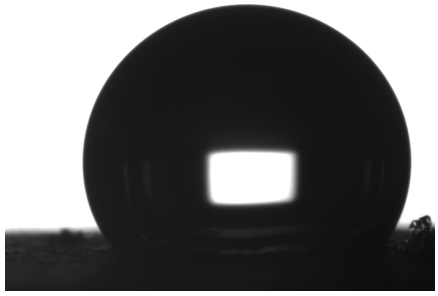

(c) 15 minutes after deposition.

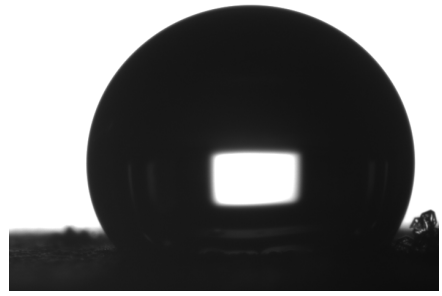

(d) 20 minutes after deposition.

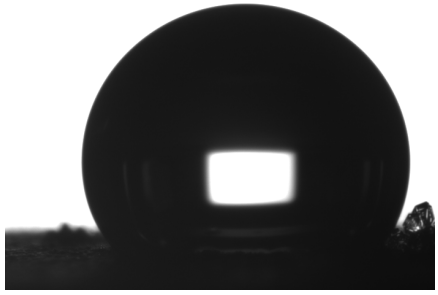

(e) 25 minutes after deposition.

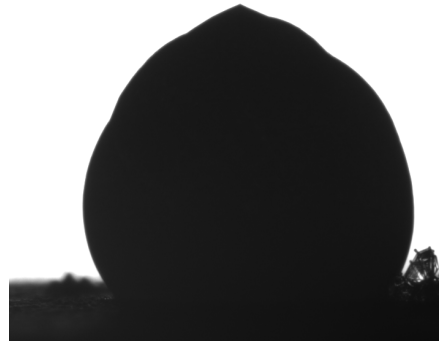

(f) 28 minutes after deposition.

Figure 4.24: Pictures showing a freezing delay test performed on sample C-S1-L2. A picture was taken every five minutes until the droplet froze. A gradual growth of ice crystals on the sample surface is also visible to the right of the droplet.

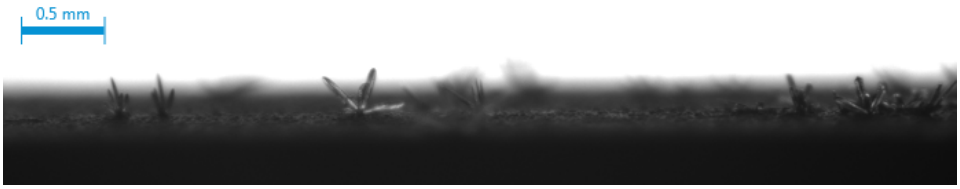

Figure 4.25: A picture showing ice crystal growth on sample F-S1-L2 while at $-10\,^{\circ}\mathrm{C}$.

4.3.3 Cyclic icing behaviour

Table 4.10 shows the results of the cyclic icing characterization done for single droplets. Table 4.11 shows the results for the three-droplet characterization. For sample C-S1-L1, the single droplet test was performed before the three-droplet one. An increase in nucleation temperature can be seen for most samples during the cyclic icing characterization, with F-S1-L4 and C-S0-L0 as notable exceptions.

Table 4.10: A table showing the nucleation temperature for the cyclic icing characterization done with one droplet.

Sample name	Cycle number	Freezing temperature [°C]
C-S1-L1	1	−9.7
	2	−5.4
	3	−9.3
C-S1-L2	1	−11.2
	2	−11.4
	3	−8.5
	4	−7.7
C-S0-L0	1	−3.0
	2	−3.2
	3	−3.8

Table 4.11: A table showing the nucleation temperature for the cyclic icing characterization done with three droplets. The freezing temperature for each of the three droplets are shown under the columns for each area. The average freezing temperature of each cooling cycle is shown in the rightmost column. The variance is the standard deviation of the three results per cycle.

		Freezing temperature [°C]			
Sample name	Cycle number	Area 1	Area 2	Area 3	Average
F-S1-L1	1	−9.9	−9.5	−6.7	-8.7 ± 1.7
	2	−6.4	−6.2	−6.4	-6.3 ± 0.1
	3	−4.8	−4.7	−4.7	-4.7 ± 0.1
F-S1-L2	1	−10.1	−10.1	−10.1	−10.1
	2	−6.6	−6.7	−6.5	-6.6 ± 0.1
	3	−4.8	−5	−5	-4.9 ± 0.1
	4	−4.1	−4.1	−4	-4.1 ± 0.1
F-S1-L3	1	−10.1	−10	−10	-10.0 ± 0.1
	2	−9.9	−10.1	−10.1	-10.0 ± 0.1
	3	−10.2	−10.1	−10.1	-10.1 ± 0.1
	4	−9.2	−9.2	−9.2	−9.2
F-S1-L4	1	−7.5	−7.3	−7.4	-7.4 ± 0.1
	2	−8.8	−9.0	−9.3	-9.0 ± 0.3
	3	−11.2	−11.1	−11.2	-11.2 ± 0.1
	4	−10.4	−10.4	−10.3	-10.4 ± 0.1
F-S2-L3	1	−12.8	−12.1	−14.3	-13.1 ± 1.1
	2	−13.1	−12.8	−12.5	-12.8 ± 0.3
	3	−12.8	−13.2	−15.5	-13.8 ± 1.5
	4	−13.1	−12.7	−15.1	-13.6 ± 1.3
F-S0-L2	1	−8.8	−8.8	−8.8	−8.8

Continued on next page

Table 4.11 – Continued from previous page

		Freezing temperature [°C]			
Sample name	Cycle number	Area 1	Area 2	Area 3	Average
	2	−4.2	−4.1	−4.2	-4.2 ± 0.1
	3	−4.4	−4.5	−4.4	-4.4 ± 0.1
C-S1-L1	1	−6.2	−6.9	−6.2	-6.4 ± 0.4
	2	−5.8	−6.5	−5.8	-6.0 ± 0.4
	3	−6.1	−6.6	−6.1	-6.3 ± 0.3
C-S1-L3	1	−8.0	−5.4	−8.3	-7.2 ± 1.6
	2	−7.5	−7.3	−6.4	-7.1 ± 0.6
	3	−8.7	−7.3	−7.8	-7.9 ± 0.7
	4	−7.5	−5.7	−7.7	-7.0 ± 1.1

Contact angle development over several icing cycles

The static CA of a droplet deposited on a sample varied considerably during the cyclic icing characterization. An example is shown in figure 4.26 for sample C-S1-L1. Similarly to the nucleation temperature characterization, the CA can be seen to decrease during cooling, until the droplet freezes. When the sample is heated back up to 5 °C and the droplet melts, it has a reduced CA compared to the angle measured during the first cycle. It is decreased even further at the start of the third cycle. However, the total CA decrease with cooling is lower for each cycle.

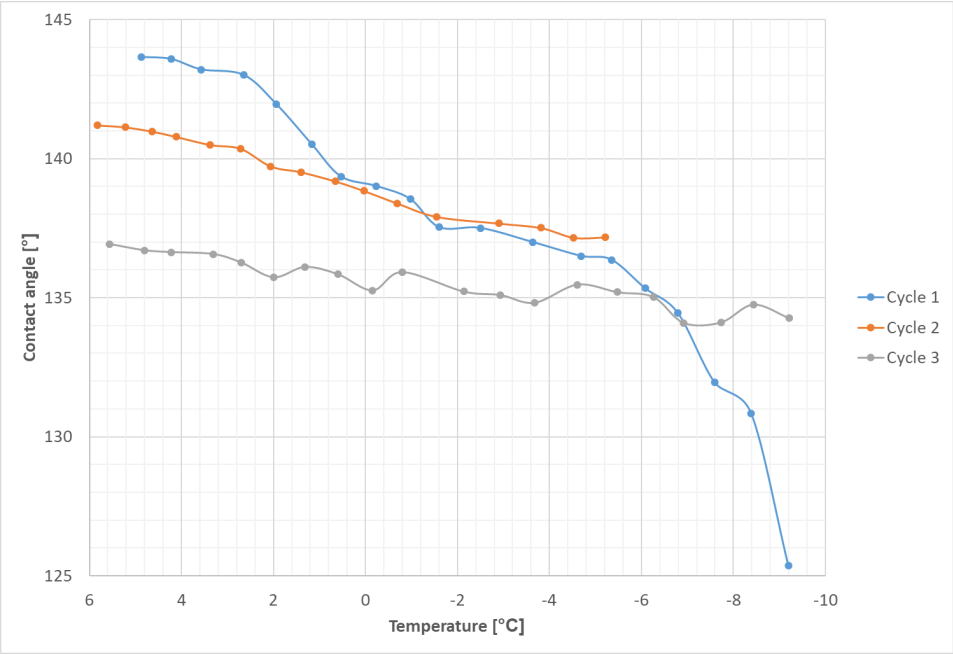

Figure 4.26: The static contact angles measured for a droplet during a single droplet cyclic icing characterization on sample C-S1-L1. The contact angles for each cycle are shown, from approximately 5 °C to freezing.

4.3.4 Coating durability

The contact angles that were remeasured on sample C-S1-L1 are shown in table 4.12. The contact angle hystereses are shown in table 4.13. A nucleation temperature of $-7.6\,°C$ was recorded for the sample.

Table 4.12: A table showing the static CA measured on sample C-S1-L1 after being subject to icing characterization.

	Contact angle [°]			
Sample name	Area 1	Area 2	Area 3	Average
C-S1-L1	162.4 ± 0.2	162.7 ± 0.4	164.3 ± 0.5	163.1 ± 0.9

Table 4.13: A table showing the ROA and CAH for sample C-S1-L1 after being subject to icing characterization.

Sample name	Roll off angle [°]	Contact Angle Hysteresis [°]
C-S1-L1	9.3 ± 6.3	27.6 ± 20.7

Chapter 5

Discussion

5.1 Substrate treatment

5.1.1 Effects of sandblasting

It is natural to compare the roughness observed on the sandblasted aluminium 5052 substrates with the values found by Vassmyr[1] on steel 316 substrates. Vassmyr used exactly the same types of sand and sandblasting machine, and so the only parameters that could differ except substrate material are the time spent sandblasting each substrate, and the distance from the nozzle to the substrate. A larger roughness is expected on the aluminium substrates, because aluminium 5052 has a hardness of 62 HB[80, pp. 674], while steel 316 has a hardness of 149 HB[81]. Vassmyr observed a $1.6 \pm 0.2\,\mu m$ and $1.59 \pm 0.06\,\mu m$ average roughness for finely sandblasted substrates, compared to the $2.83 \pm 0.15\,\mu m$ found in this work. There is thus a clear increase in roughness for the aluminium substrates compared to steel. The increase is even larger for coarsely sandblasted substrates. Vassmyr got $4.8 \pm 0.2\,\mu m$ and $3.6 \pm 0.9\,\mu m$ average roughness. While the roughness could not be precisely determined on the aluminium substrates because it was too large for the instrument, it was found to be over $7\,\mu m$ and is thus an even larger increase than for finely sandblasted substrates.

5.1.2 Silica particle deposition

The silica particles seem to have been deposited relatively unevenly on the sample surfaces. Figure 4.3 shows an area with a very thick deposition of particles, but with a less dense deposition on outlying areas. This deposition seems to cover up any underlying microroughness on the aluminium surface, and therefore suppresses the intended hierarchical roughness.

However, outside the larger agglomerates, the particle deposition covered the microstructured surface more evenly. Figure 4.4 shows areas where the particles have been deposited along the features of the microstructure. Some variation can still be seen, with a thinner layer in the valley in the upper right. It is likely that the microstructure prevented a completely even silica particle deposition. Even so, the resulting surface appears to have a hierarchical roughness, with a microstructure of sandblasted aluminium, and a layer of silica nanoparticles providing nanoroughness.

Effect of silica particle deposition speed

In this work, the silica particle sol deposition speed was varied as a parameter. Sample F-S2-L3 had a deposition speed of 0.5 mL/min, compared to the standard 1 mL/min used for most samples. With a reduced deposition speed, a smaller density of deposited silica particles on the surface is expected. This is seen to be the case when comparing the SEM images for sample F-S2-L3 in figure 4.8 with the SEM image for sample C-S1-L3 in figure 4.7, which had a standard particle deposition. Sample F-S2-L3 seems to have a lower coverage of silica particles, and less complete particle layers. Though it should be noted that there is density variation on F-S2-L3 as well, as seen in figure 4.8b.

Silica nanoparticle size estimation

The size of the silica nanoparticles synthesised in this work was estimated to be 186 ± 12 nm. This can be compared to the nanoparticle sizes found by Vassmyr[1] and Luneng[2], as they followed the same synthesis route and used the same experimental parameters. Vassmyr estimated her particle sizes to be 261 ± 26 nm, while Luneng found his particle sizes to be 221 ± 8 nm. The particles were thus found to be somewhat smaller than in Luneng and Vassmyr's works.

The difference may be caused by several factors. For example, the rate at which TEOS was added to the reaction solution was not specified, and likely differed. The Masalov growth model[74] for silica nanoparticles says that the growth happens in several stages. Silica particles appear and grow when TEOS is added to the reaction solution. Adding more TEOS will lead to new, smaller particles being formed, which will join to the existing particles. That means a new growth stage takes place whenever more TEOS is added, as shown in figure 2.8. Varying the rate at which TEOS is added, and volume of each dose, will therefore change the growth of the particles. Then, the final porosity and size of the final particles would also be affected.

Another reason for the difference in results could be the size estimation itself. The nanoparticle size estimation in section 4.1.4 was based on the particles shown in the SEM image in figure 4.9. The estimation was based on comparing the apparent size of the particles with a set scale for an image. This related the pixels to an actual physical size. The image scale was set based on the scale bar provided by the SEM

software for that magnification. However, the scale of the image still had to be set based on a manual measurement of the scale bar in ImageJ. Inaccuracy in setting the scale could therefore introduce a systematic error in all the size measurements. A second possible source of uncertainty was the focus of the SEM image. The particles were not in perfect focus, which made it difficult to see their outlines. The particle size would therefore have been over- or underestimated by a few pixels in certain cases.

The surface roughness involved would also have affected the size estimation. The accuracy of the size estimation depended on the relative height of the surface on which the particles are placed. Particles which were placed higher will appear larger, and vice versa. The particular SEM image in figure 4.9 was chosen because the surface was relatively flat, to make the size estimation more accurate. However, a certain roughness is still visible in the image. Additionally, the surface seems to have a certain slope, which would further worsen the accuracy of the size estimation.

5.1.3 Fluorosilane sol deposition

Because the fluorosilane coating could not be imaged in SEM, an evaluation of the coating coverage or quality could not be performed. The coating thickness was uncertain, but was expected to be thin from the cross section SEM images. Additionally, the coating may have been partly torn off during polishing. It is therefore difficult to conclude to what degree the coating may have covered up the micro- or nanostructure. But based on the interface visible in figure 4.12, both the micro- and nanoroughness seem to have been preserved. The SEM images of C-S1-L3 (figure 4.6 and 4.7) and F-S2-L3 (figure 4.8) show that the silica nanoparticles are still very evenly distributed after fluorosilane coating.

However, it is possible that the fluorosilane coating had its own inherent roughness. The fluorosilane sol-gel was base catalyzed, which would promote agglomerate formation during the synthesis. These agglomerates would later cross-link to form a rough coating[67]. These agglomerates could potentially have introduced more roughness on the surface. The form of this roughness was unknown, though from the cross section SEM image it seems any inherent roughness would exist on the nanoscale rather than microscale. Crucially, its interaction with the existing surface nanoroughness provided by the SEM particles is unknown, and would be natural to investigate further.

5.2 Hydrophobicity characterization

5.2.1 Contact angle measurements

Generally, the static contact angles for coated samples trended around 160°. A significant increase in contact angles compared to uncoated substrates (F-S0-L0, C-S0-L0, U-S0-L0) was observed. The contact angle was also increased by 55° or more with the introduction of microroughness through sandblasting and silica nanoparticles. The substrates that were only coated with fluorosilane and not silica particles, i.e. F-S0-L2 and C-S0-L2, had average contact angles around 155°. More precisely, without silica particles, there was a 6.4° CA decrease for coarsely sandblasted substrates, and 4.4° CA decrease for finely sandblasted substrates. The finely sandblasted substrate with reduced silica particle deposition, F-S2-L3, had an average CA very close to the finely sandblasted substrate with more particle deposition, F-S1-L3, though with very high variance. These results indicate that the nanoroughness offered by the silica particles make a noticeable difference in the CA. To understand why, the contact mode on the surfaces has to be discussed.

According to Quéré[38], it is very improbable that droplets on a surface with a significant roughness will be purely in the Wenzel contact regime. Especially so when the surface has a low surface energy, which was the intention of the fluorosilane coating. Additionally, some coarsely sandblasted samples demonstrated low ROA and CAH, which would be impossible in a strict Wenzel regime. It is therefore more likely that droplets existed primarily in a mixed state, or the Cassie-Baxter state. From equation 2.5, it is known that the apparent contact angle θ^* for droplets in the Cassie-Baxter regime depends on the surface fraction Φ_s. By reducing Φ_s, θ^* is increased, and an increased CA is measured. It seems likely that the deposited silica particles increased the air trapping under the droplet, and therefore increased Φ_s.

If this interpretation is correct however, one would expect a higher contact angle for the substrate with reduced silica particle deposition. Less particles should allow for an even smaller contact area with the surface, as there is less of a complete layer of particles. This is assuming there are enough silica particles there to maintain the air trapping effect in the first place. It is worth noting that F-S2-L3 actually did exhibit a larger contact angle than F-S1-L3 on area 1 and 2, but had a 10° lower CA on area 3. The low result on area 3 may have been caused by uneven silica particle or coating deposition. If there was a significantly lower silica particle deposition on area 3, the wetting behaviour would have been more similar to the substrate with no silica particle deposition, F-S0-L2, which had a CA of $155.9 \pm 4.0°$.

Other general trends that can be observed is that coarsely sandblasted substrates have higher CA than their finely sandblasted counterparts, with lower variance. This is reasonable when considering that an increased roughness would reduce the water/solid surface contact area. Another trend is that samples with more coating layers have reduced average CA. However, the variance in the measurements is

large enough that no conclusion can be drawn about any correlation. One notable exception to the aforementioned trends is sample F-S1-L4, a finely sandblasted sample with 4 fluorosilane coating layers. It is unclear why this sample had a markedly higher CA than other samples with less coating layers. It also draws into question the validity of the trends discussed here.

Sources of uncertainty in contact angle measurements

Several sources of uncertainty may have affected the CA results, and should be taken into consideration. One example is the humidity at the time of measurement. The CA measurements were always done in ambient laboratory conditions. That means at a temperature of approximately 22 °C to 24 °C. Humidity on the other hand was not controlled for, and may have been a wide range of values. It is expected that the advancing CA would decrease with increasing humidity[82]. Vassmyr[1] also observed variations in CA with humidity on the order of 3°. Both an increase and decrease in CA was seen with increasing humidity, so no definitive correlation was shown.

Additionally, the baseline placement may have introduced uncertainty in the contact angle results. The baseline was set manually through identifying the actual contact line between droplet and surface in the image. For samples that were not sandblasted, identifying the correct baseline was difficult because it was very reflective. Setting the baseline a few pixels higher or lower could vary CA by approximately 2° to 3°. This means there may be significant deviation between the reported results and the actual results. Such a considerable element of uncertainty may make several apparent correlations between experimental parameters and resulting CAs invalid.

Any imprecision in setting the baseline would also affect the droplet volume estimation. The droplet volume estimation was based on two parameters: the baseline, and the diameter of the droplet depositing needle. The measurement of the needle was assumed to be precise, as it was done physically with a micrometer. However, the diameter then had to be compared to the apparent size of the needle on the Advance camera feed. Setting the needle size wrong would make the software over- or underestimate the size of the droplet. The baseline was used by the software to estimate the size of the droplet, and setting it too high or too low would also introduce errors to the size estimation. In addition, some variance in the actual deposition volume should be expected.

The combination of these factors would have contributed to the $\pm 2\,\mu L$ variance in the size estimation. However, the uncertainty introduced was not random, but systematic. The needle diameter was set once per measurement session, and the baseline on a droplet to droplet basis. That means comparing droplet volumes between different droplets and sessions would introduce uncertainty. But measuring volumes for a specific droplet multiple times would avoid this uncertainty. Thus any trends of decreasing or increasing droplet volume for the same droplet could be considered reliable, such as the one shown in figure 4.17.

5.2.2 Contact angle hysteresis measurements

It was established in section 2.2.2 how a certain surface roughness is necessary to achieve small CAH and ROA. The droplet should be in the Cassie-Baxter contact mode, resting on the surface asperities and the air trapped beneath it. The hysteresis results show that only the coarsely sandblasted substrates had any notable ROA and CAH. Therefore, it is likely the coarsely sandblasted substrates were more easily able to maintain the Cassie-Baxter contact mode compared to finely sandblasted substrates. The larger roughness would increase the air trapping under the droplets. The roughness values and the SEM images in figure 4.5 imply that there was a greater height difference between hills and valleys in the surface topography for the rougher substrates. If the droplets rested mostly on the surface asperities, it would have been harder to penetrate into the pits on coarsely sandblasted substrates. In that case, the defects per unit area ϕ_s that the droplet encounters will be low, and the CAH will be reduced as well, per equation (2.8).

However, a surface with greater average roughness does not necessarily have a smaller CAH, despite seemingly being the case here. Extrand[83] argues that the shape of the microscale topography is much more important than simply its roughness. Different surfaces can exhibit either very large or very small CAH depending on the topography, even though they both have large roughness per se. For example, if the surface asperities are too far apart, the droplet can collapse into the pits between the asperities. The surface becomes unable to suspend the droplet, and the liquid/solid contact area will increase. This will make the contact line pinning stronger and increase the CAH of the droplet.

The lower water/solid surface area should also result in a larger static contact angle. From the Cassie-Baxter equation (2.5), it is known that the apparent static contact angle increases with reducing Φ_s, which is the water/solid surface area. Larger static contact angles is in fact observed for most coarsely sandblasted substrates compared to finely sandblasted substrates. However, the significant uncertainty in the contact angle results, as well as the finely sandblasted substrate with four coating layers having the second largest contact angle, makes it difficult to connect the CA and CAH results through the Cassie-Baxter equation.

If the droplets on the finely sandblasted substrates were in a mixed contact mode instead, its CA would also be governed by the roughness factor r in equation (2.4) and (2.6). As Φ_s and r were unknown, nothing conclusive can be said about the contact modes on finely and coarsely sandblasted substrates and the resulting contact angles.

It should be noted that several authors in literature have found the Cassie-Baxter and Wenzel equations to be inaccurate, especially for surfaces with complex topographies [37], sharp edges[83], or surface chemical/topographical inhomogeneities [84][85]. Using the Cassie-Baxter equation for superhydrophobic surfaces have been cautioned against[86]. Improvements to the equation have been proposed to enable a prediction of hysteresis[87]. The apparent disconnect in the CA and CAH results

according to the Cassie-Baxter equation are thus not out of the norm.

Another source of uncertainty are the possibility of metastable Cassie-Baxter states. If some substrates exhibited a metastable state, the force that the droplets were deposited with may have pushed the droplet partly into the surface topography. This scenario was discussed by Quéré et al.[38], and took a force of 200 Pa in their example. The deposition force was decided by how gently the needle with the droplet was lowered, and was not standardized. This would have resulted in a greater degree of Wenzel states on certain samples and a ROA higher than 90°.

5.2.3 Reduction in contact angle with temperature

The contact angle θ, measured at room temperature, was used as a parameter to define the hydrophobicity of the substrates. However, a large decrease in the CA was observed with decreasing temperature for several coated samples, both from 22 °C to 5 °C, as well as from 5 °C to nucleation. This behaviour was also observed by Vassmyr[1], as well as by other authors in literature[32][64]. If the hydrophobic properties drastically decrease at lower temperatures, the ability of a hydrophobic surface to prevent water from freezing on the surface would be reduced. The insulating air layer between droplet and surface would be reduced or removed entirely. Classical nucleation theory implies that a smaller contact angle decreases the energy barrier for icing. This would be counter-productive, as the surface has to be used at low temperatures for anti-icing applications.

An influencing factor on the change in contact angle during cooling was likely the evaporation of the droplet. It has been discussed in section 2.2.2 that the evaporation of a droplet reduces its contact angle, unless on a surface with very low contact angle hysteresis. The Advance software also measured a decrease in the droplet volume during cooling from 22 °C to 5 °C, shown in figure 4.17. The reduction in volume per degree of cooling gradually decreases as the temperature is lowered. However, the evaporation rate seems to have been higher for the sandblasted substrate compared to untreated. Both volumes end up relatively constant closer to 5 °C, but the droplet deposited on the sandblasted substrate loses some more volume in the process. It is therefore expected that evaporation played a greater role in the reduction of contact angle for the sandblasted substrate, compared to the untreated. As it was found that the sandblasted substrate had a greater reduction in contact angle during cooling, the influence of evaporation may be worth further investigation.

The difference in evaporation rates between the sandblasted substrate and untreated substrate can be explained by the difference in hydrophobicity. The sandblasted substrate is clearly more hydrophobic, demonstrating a larger CA. Droplets with a larger CA has a more spherical shape, and reduced contact area with the surface. Instead, the droplet will have a greater surface area towards air. It may then seem reasonable that the evaporation rate is larger on hydrophobic surfaces. Similar results have been found in literature, for example by Hu and Larson[88]. They

found that an increased contact angle of an initial droplet would lead to increased evaporation rates. However, their model was only developed for contact angles between 0 and 90 degrees.

Another factor which may have influenced the difference in evaporation rates is the cooling rate for the two droplets. In the theory section, it was explained how the small water/solid contact area on hydrophobic surfaces was a beneficial anti-icing property. The small contact area reduces the heat transfer rate from water, which lets a droplet remain at higher temperatures for longer. If a droplet remains at higher temperatures, its evaporation rate will also be larger. Thus the droplet deposited on the sandblasted sample may have had increased total evaporation because it cooled slower than the droplet on the untreated sample.

However, the evaporation rate of the droplet flattened out as it approached 5 °C, and was almost non-existent at lower temperatures. Clearly, another phenomenon caused the reduction in CA at these temperatures. Heydari et al.[32] attributes the reduction in CA at lower temperatures to the condensation of humidity. As the air in the chamber is cooled, its vapour pressure is reduced. At that point, air will start to condense instead of evaporate. A certain evaporation still happens from the droplet because of its curved surface driving a pressure difference, but it has been shown to be minimal. The vapour will condense on cold surfaces in particular, including the sample.

Simplified, the air layer surrounding a droplet will be saturated with vapour, and the vapour will spread through diffusion[88]. Therefore, it is expected that condensation will be more extensive in the areas immediately surrounding the droplet, including at its triple-phase contact line. The supersaturation and condensation will modify the solid-vapour and solid-water interfacial energies, leading to a reduced CA[61]. Condensation will also happen within the air pockets between the surface asperities, which the droplet on a rough, hydrophobic surface rests upon. Thus a gradual transition to the Wenzel contact mode will occur, with accompanying CA and CAH decrease. This is illustrated in figure 5.1.

The transition to the Wenzel contact mode explains why a much larger CA decrease is seen for the rough sample compared to the smoother sample. It also explains why the CA decrease seem to be divided into two stages. The first stage is driven by evaporation, with a slow CA decrease until around 12 °C. And the second stage is where the condensation began, leading to a much faster CA decrease. The significant CA decrease at sub-zero temperatures is also explained by the humidity condensing. Ambient humidity levels were present in the chamber before reducing the temperature, which would start to condense at lower temperatures. The higher CA for coarsely sandblasted substrates compared to finely sandblasted ones when cooling is likely because their initial CA were higher, and that there was more room for condensation within their microstructure. Coarsely sandblasted substrates would then be more resistant to a change in wetting state through condensation.

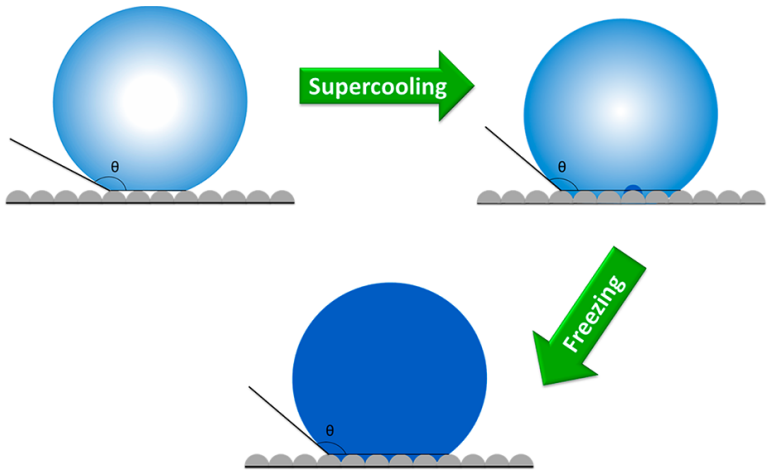

Figure 5.1: An illustration of the origin behind the CA decrease for rough, hydrophobic surfaces as the temperature is lowered. From [32].

5.3 Anti-icing characterization

5.3.1 Nucleation temperature

Generally, the nucleation temperatures can be divided into three levels, or tiers. The samples within each tier had relatively similar nucleation temperatures, although there were still variations within each tier. The first tier are the uncoated samples U-S0-L0, C-S0-L0 and F-S0-L0, which had nucleation temperatures in the range of $-3.1\,°C$ to $-4.2\,°C$. The second tier are the fluorosilane coated samples, both with no silica deposition and a standard silica deposition ($1\,mL/min$). These results are grouped in the interval of $-7.7\,°C$ to $-10.7\,°C$. The nucleation temperature results within this tier are not necessarily all equal, but the results have to be viewed in context with the uncertainty of the measurements. Several substrates exhibited variances in results that spanned across the entire range of this tier. The measurement method was also expected to cause uncertainty in the measurements, which will be expanded upon further. Hence, any conclusions based on the $2\,°C$ to $3\,°C$ differences in nucleation temperature within this tier are not justified. The substrate with reduced silica particle deposition has to be placed into a third tier, because of its lower nucleation temperature of $-13.1 \pm 1.1\,°C$.

The fluorosilane coating lowered the nucleation temperature significantly. Applying the fluorosilane coating reduced the nucleation temperature by at least $5\,°C$, independent of both sandblasting and silica particles. The increased hydrophobicity from the sandblasting or the silica nanoparticles did not translate into a lower nucleation temperature. For example, sample U-S0-L2, which was not sandblasted but only coated with fluorosilane, had a nucleation temperature of $-10.7 \pm 2.9\,°C$, which was lower than most other coated substrates despite large variance. The middle area had a nucleation temperature of $-14\,°C$, which was as low as some nucleation temperatures on the finely sandblasted sample with reduced particle deposition. These results were achieved despite a room temperature CA of only $99 \pm 8°$. Therefore, no correlation between hydrophobicity and nucleation temperature was found. Any effect the insulating layer of air would have had was negated by the change in wetting state at lower temperatures. In addition, these results seemingly contradicts the prediction from classical nucleation theory in equation (2.12). Here, a larger CA would lead to a larger energy barrier for icing.

However, this disagreement is not out of the norm compared to existing literature. Eberle et al.[59] found relatively constant nucleation temperatures across a wide range of both CA and roughness values. They explained this through expanding on the classical nucleation theory, by postulating a quasi-liquid layer under the nucleus. Furthermore, the importance of the surface nanostructure was underlined. To arrive at equation (2.12), it was assumed that $R_s > 10r_c$. But if the surface radius of curvature R_s is close to the critical ice nucleus radius r_c, a strong ice suppression effect is expected.

The silica particle diameter was found to be $186 \pm 12\,nm$, compared to $r_c = 9.1\,nm$

at $-5\,°C$ and $r_c = 4.5\,nm$ at $-10\,°C$. The particle radius is therefore too large to suppress ice nucleation. Theoretically, smaller silica nanoparticles may have suppressed ice nucleation more effectively. The findings of Cao et al.[55] supports this recommendation. They tested the anti-icing properties of a superhydrophobic particle-polymer composite with different particle sizes. They found a greater ice suppressing effect when using smaller, nanometer-sized particles. The fluorosilane coating may also have had a certain nanoscale roughness, which could have helped suppress nucleation.

But importantly, the surface homogeneity is very important for ice suppression. There is a possibility that a few areas of the substrates had nanostructures that strongly suppressed ice nucleation. However, as long as there also were more flat areas where $R_s > 10r_c$, ice nucleation would be favoured in these areas[21]. It is therefore unlikely that the ice suppression effect of small nanostructures affected the nucleation temperatures.

The nucleation temperature for the sample with reduced silica particle deposition is promising. But its low nucleation temperatures cannot be properly understood without further knowledge of the nanoroughness as a result of the nanoparticles and coating, and how varying the silica particle concentration will change the nanoroughness.

To investigate the influence of aluminium as a substrate material compared to steel, the nucleation temperatures can be compared to the ones found by Vassmyr[1]. She found a nucleation temperature of $-9.5\,°C$ for a sample that underwent the same surface treatment as F-S1-L2, which had a nucleation temperature of $-9.9 \pm 0.4\,°C$. Moreover, she found a nucleation temperature of $-6.1\,°C$ for the same treatment as C-S1-L2, with a $-9.7 \pm 1.4\,°C$ nucleation temperature. The nucleation temperature was very close for F-S1-L2, yet showed a large difference for C-S1-L2. No variance was given, and so a precise comparison is difficult. One explanation for the difference could be the microroughness. The same sandblasting resulted in a different microroughness on aluminium compared to steel. Nevertheless, the microroughness type did not result in large differences in nucleation temperatures for other samples in this work. It is unknown whether the large difference in results for sample type C-S1-L2 is caused by the substrate material.

Uncertainty in the nucleation temperature measurements

In general, substrates exhibited variances in nucleation temperatures of up to $\pm 2\,°C$, or $\pm 3\,°C$ in the case of the substrate which was not sandblasted. Eberle et al.[59] also found that most of their nucleation temperatures spanned over $2\,°C$ to $3\,°C$ despite a very different surface and a median nucleation temperature closer to $-22\,°C$. Hence, some uncertainty could perhaps be attributed to the nature of the nucleation temperature experiments, though it can certainly be decreased further.

A significant source of uncertainty for the nucleation temperature measurements was the way the temperature was measured. It was shown in figure 4.22 that

there was a large difference between the actual measured temperature and the temperature of the Peltier element. The temperature sensor was taped down to stay in contact with the Peltier surface which the substrates were resting on. Despite this, the temperature sensor is expected to measure a combination of air and surface temperature. Heydari[32] found that the temperature decrease in air was much slower than the surface temperature decrease during their cooling experiments. This depends on the environment that the measurements were performed in, such as the amount of air in the chamber and cooling rate, and would be expected to be different for this work. Even so, it is still reasonable to expect that the air temperature remained warmer for longer during cooling. Hence, the measured temperature would likely also be larger.

This puts into question the nucleation temperature results. However, since the same thermostat cooling rates were used across all experiments, the same difference between the measured temperature and the surface temperature would be expected. Therefore, any trends in increasing or decreasing nucleation temperatures across substrates would not be invalidated. That means the conclusion that there is no correlation between hydrophobicity and nucleation temperature still holds as well.

5.3.2 Delay of icing

A delay of ice formation was only observed for certain fluorosilane coated substrates with silica particles. The greatest delays observed were 43 min and 28 min for the coarsely sandblasted substrates with 1 and 2 coating layers, compared to the approximately immediate freezing on most other substrates. Interestingly, the coarsely sandblasted substrates with the longest freezing delays did not have any lower nucleation temperatures than substrates without any delay, indicating that other factors govern delay of icing. The only exception is sample F-S2-L3, the finely sandblasted substrate with reduced particle deposition, which also had particularly low nucleation temperatures.

Several authors have shown that a reduction in contact area will increase the freezing delay time for hydrophobic surfaces[22][59]. The results found in this work seem to support this conclusion. Some of the most hydrophobic substrates also experienced the longest freezing delays. In particular, the coarsely sandblasted substrates that retained a higher CA at lower temperatures showed long delays of freezing, as shown in figure 4.7 and 4.9. Their higher CA likely implied that they had transitioned less to the Wenzel regime because of condensation. That would also imply that the droplets had a smaller contact area with the surface than on substrates with smaller CA. If this interpretation is correct, it would also mean a correlation exists between hydrophobicity and anti-icing in this instance.

However, some results contradict this. For example, samples F-S1-L1 and F-S1-L2 had longer delays than sample C-S1-L3, but much smaller CA at low temperatures. Further experiments need to be undertaken to confirm or deny a correlation. In addition, there is reason to suspect significant uncertainties in the freezing delay

measurements caused by environmental conditions. Extensive ice crystal growth was observed on the substrates at −10 °C, and resulted in a different freezing mechanism with immediate nucleation. This phenomenon will be expanded upon to investigate its influence.

5.3.3 Freezing mechanism

Two visibly different freezing mechanisms were observed during this work. The first was observed primarily during the nucleation temperature characterization, shown in figure 4.20. Here, the droplet quickly turned opaque at a certain temperature. The process is discussed in Oberli et al.[61], and is believed to be a rapid kinetic crystal growth from the initial point of nucleation. The rapid growth continues until the droplet reaches 0 °C. Other authors report that the frozen shell forms in approximately 20 ms to 40 ms[21][60], though this could not be precisely verified in this work. Different explanations for the non-transparency of the droplet have been offered[61]. It has been suggested that the release of air bubbles or light scattering may be the origin of the effect. It has also been proposed that a solid ice shell forms around the droplet, with a still liquid interior. If the ice shell interpretation is correct, it also explains the deformation that appears in the upper profile of the droplet. The upper part of the ice shell will be pushed outwards because of the volume expansion associated with the phase transition from water to ice.

The second freezing mechanism was only observed during the delay of ice formation experiments. Here, the frozen droplet is very transparent, with the occasional appearance of what seemed to be air bubbles. This can be seen in figure 4.23. For these droplets, no opaque outer shell forms when they freeze. This may be the reason why no deformation is visible in the upper droplet profile, unlike for the first freezing mechanism. When no outer shell forms, there is no deformation as the water expands in volume while freezing. The reason the droplet did not turn opaque in the first place is because of ice growth on the surface. This freezing mechanism could deliberately be provoked by depositing a droplet on an existing ice crystal. The nucleation energy barrier was likely drastically lowered, and the crystal functioned as a nucleation site. The droplet started freezing immediately upon contact with the nucleation site, and thus did not have time to become supercooled. The droplet therefore did not go through a kinetic crystal growth step.

The substantial ice crystal growth at −10 °C often prevented characterization of the surface itself. Occasionally, it also disturbed the gentle balance of the supercooled droplets resting on a surface without freezing. One example is shown in 4.24, where the ice crystal on the right may have grown until it came into contact with the droplet.

Despite trying to avoid depositing droplets on ice crystals, it is likely that microscopic crystals still covered the surface, forming a layer of frost. Oberli et al.[61] found that micrometer-sized droplets formed on their hydrophobic surfaces at temperatures around 1 °C and below, and started growing through a process equivalent

to Ostwald ripening. Once one of the droplets froze, dendritic ice crystals started growing out from the droplet. If these crystals came into contact with another droplet, nucleation was initiated. Thus frost started spreading on the surface, which made droplets they deposited freeze prematurely.

It is likely that the same process happened in this work. Vapor droplets would have fit inside the microstructure of the surface and formed in the Wenzel regime. They would then have had a lower energy barrier for nucleation and started freezing, thus forming frost on the surface. Frost formation may therefore have affected the results obtained during the delay of icing experiments. The frost formation would have been greater at higher humidity levels, which could not be controlled below 5 °C. It has however been demonstrated that certain superhydrophobic surfaces delay frost formation in literature[89]. Unfortunately, there was no way of tracking the frost formation on the substrates. That means droplets may have nucleated far earlier than would otherwise be the case. Therefore, it is very difficult to draw conclusions from the icing delay results. Simply ensuring that the first freezing mechanism was observed instead of the second would not be enough to ensure no deposition on microscopic nucleation sites. The freezing mechanism was believed to result from how supercooled a droplet was, and the droplet temperature before deposition was not controlled.

5.3.4 Cyclic icing behaviour

The substrates showed a wide variety of behaviours during the cyclic icing tests. Most substrates experienced an increase in nucleation temperatures, some remained stable, while sample F-S1-L4, which was finely sandblasted and with 4 coating layers, showed a decrease. Other than the finely sandblasted substrates with the fewest coating layers showing the largest increase during the cyclic tests, no apparent trend appears. The CA of the droplet on substrate C-S1-L1 decreased each cycle as seen in figure 4.26, likely because of a transition to the Wenzel contact mode through condensation.

The cause of the large variances between cycles may be the uncertainty in the nucleation temperature experiments, similarly to what was discussed in section 5.3.1. However, there was much less variance in the temperatures where each droplet froze during the three-droplet measurements. They generally stayed within 1 °C from each other per cycle. The small variance may have originated from frost spreading across the substrate surface. Once one droplet froze, frost would have spread out from that droplet. The frost may have made the other droplets freeze prematurely, similarly to the problems experienced by Oberli et al.[61]. The additional two droplets may have also increased the humidity levels in the chamber, and thus led to increased condensation. Another explanation for the small variance is relatively homogeneous substrates. In that case, the general 2 °C to 3 °C uncertainty would simply reflect the variance in the nucleation temperature measurements. Further experiments with better control of the humidity levels and thus frost formation would have to be conducted to clarify.

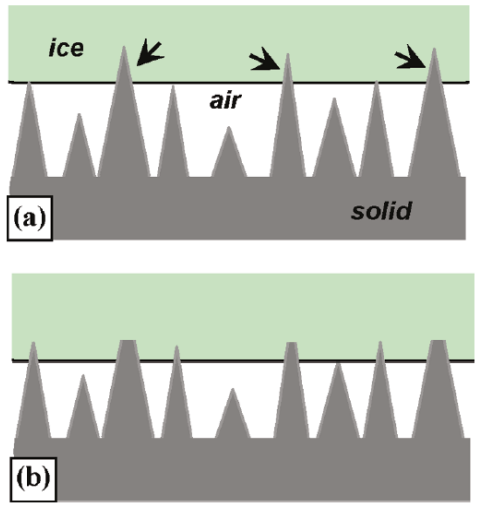

Figure 5.2: Illustration of surface roughness degradation through icing. In (a), the upper asperities of the roughness are indented into the ice. In (b), some asperities have been damaged, increasing the droplet and ice contact area. From [57].

But how can the significant increase in nucleation temperatures for the finely sand-blasted substrates with one and two coating layers be explained? These substrates eventually reach similar nucleation temperatures to the uncoated substrates. The increase thus seem to be outside the expected uncertainty for nucleation temperature measurements. In addition, an large increase was found for substrate C-S1-L1 when comparing its nucleation temperature of $-9.9\,^{\circ}\mathrm{C}$ with the first cycle of its cyclic icing behaviour, which was $-6.4 \pm 0.4\,^{\circ}\mathrm{C}$.

An explanation for the decrease could be surface degradation. Kulinich et al.[57] found that the ice adhesion on their samples increased after several icing cycles, with an accompanying reduction in room temperature CA and CAH. They attributed this reduction to the upper asperities of the surface being caught inside the droplet as it froze. The expansion of the droplet as it turned to ice led to mechanical damage or breaking of the uppermost asperities. That means the surface was worn down, which should lead to a larger droplet/surface contact area and smaller CA, as illustrated in figure 5.2. Boinovich et al.[90] also experienced a reduction in CA over several cycles, which they attributed to changes in surface morphology and hydrolysis of their fluorooxysilane coating. In a later study, Boinovich et al. also found that some of their surface features, such as nanoparticles and nanotubes, detached from their surface when exposed to water[22].

It is possible that the surface of the samples in this work were affected in a similar manner. This hypothesis was tested through the coating durability experiments, which consisted of finding the CA and CAH on sample C-S1-L1 after icing charac-

terization. Only a 2.6° CA decrease was found, which is not conclusive. The CAH had too much variance to judge whether an increase or decrease had taken place. It should be noted that small variations in droplet placements could occur per area, which could have led to partly missing the areas which were tested upon. Though the CA decrease was small, Boinovich et al.[90] found a similar decrease for the same amount of cycles. However, it was found that the nucleation temperature remained relatively constant across multiple types of roughnesses. Hence, a degradation of the surface roughness would not be expected to increase nucleation temperatures.

But if the coating was degraded, it would have had a much larger effect on the nucleation temperatures. When water froze and expanded, coating could have been indented into the ice and removed from the surface. The result would be areas with bad coating coverage, which would be more prone to nucleation. An increase in the nucleation temperature would then be expected. But CA would not be expected to decrease much, as it is a result of surface properties over a larger area. Coating degradation would be expected to have a larger impact for samples with a thinner coating from fewer coating layers. The large increase in nucleation temperature observed for the samples F-S1-L1 and F-S1-L2, with 1 and 2 coating layers, support this notion. To confirm that coating degradation affected the nucleation temperatures, further investigations into the coating coverage would have to be performed.

Chapter 6

Conclusion

Aluminium substrates have been sandblasted with fine and coarse sand, and the resulting microstructure has been investigated. The surface roughness was found to be larger than for similarly treated steel substrates. Silica nanoparticles have been synthesised and spray coated onto substrates at varying deposition speed, and their diameter was found to be $186 \pm 12\,\text{nm}$. Their coverage was relatively even, though with some thicker deposits covering up the microstructure. A fluorosilane sol-gel was synthesised and spray coated onto the substrates in one or several layers. The result was aluminium surfaces with a hierarchical micro- and nanoscale roughness and low surface energies.

The combination of a sandblasted microstructure and fluorosilane coating proved to be necessary to achieve large hydrophobicity. The addition of silica nanoparticles increased the CA by approximately 5°, and was attributed to a reduced solid-liquid contact area. Generally, substrates with larger microroughness and less coating layers were found to have greater CA, but no conclusive correlation could be found. Only coarsely sandblasted substrates were found to have a ROA $< 90°$. The coarse microstructure was thought to be able to more effectively suspend droplets in the Cassie-Baxter contact mode. The most hydrophobic substrate demonstrated a CA of $165.7 \pm 1.3°$, a ROA of $9.2 \pm 0.6°$ and a CAH of $22.8 \pm 1.6°$. It had a coarse microstructure, standard silica particle deposition speed and one fluorosilane coating layer.

The CA was found to decrease significantly at lower temperatures. The decrease signalled a transition to the Wenzel contact mode, and an increased solid-liquid contact area. It was thought to primarily be caused by the condensation of humidity on the substrate surfaces at low temperatures.

The fluorosilane coating was found to lower the nucleation temperature significantly. Application of the fluorosilane coating decreased the nucleation temperature by more than $-5\,°\text{C}$. The lowest nucleation temperature for a substrate was $-13.1 \pm 1.1\,°\text{C}$. However, significant variance in the nucleation temperature results was found.

Taking the uncertainty into account, the nucleation temperature was found to be independent of microstructure type, whether it be untreated or sandblasted, despite having widely different CA. Only a small decrease in nucleation temperatures for a reduced silica particle deposition was observed. Thus, no correlation between hydrophobicity and nucleation temperatures was found, in agreement with literature. The lack of a correlation could not be explained by the reduction in CA at low temperatures for rough surfaces, which would remove the insulating air layer and lower the energy barrier to nucleation. It was concluded that the coating was primarily responsible for the nucleation temperature decrease, and not the micro- or nanostructure. The silica particles were found to likely be too large to effectively suppress ice nucleation. No conclusive explanation could be found for the lower nucleation temperatures observed with a reduced silica particle deposition, because the nanoroughness as a result of nanoparticles and coating was unknown. Surface homogeneity was found to be important for the nucleation temperature, especially in terms of coating coverage. Indications of surface degradation after icing was found, but could not be confirmed.

Some coated substrates were found to have long delays of ice formation compared to untreated substrates, with the longest being 43 minutes. The most hydrophobic substrates had the longest delays of ice formation, which would support a correlation between these properties. However, the correlation is contradicted by certain less hydrophobic substrates showing longer delays than other, more hydrophobic substrates. Thus, no correlation was found between hydrophobicity and anti-icing properties. In addition, the icing delay measurements were found to be significantly affected by condensation. The condensation and freezing of atmospheric humidity formed ice crystals on the substrates. A second freezing mechanism was observed for droplets on substrates with significant growth of ice crystals. These droplets had no delay of icing, and froze immediately upon deposition. Frost formation was therefore suspected to have affected the icing delay results.

Chapter 7

Further work

Despite showing good anti-icing properties, the coating and surface structure can both be improved. The effects of a reduced silica nanoparticle deposition should be further investigated. Smaller silica particles should be tested to exploit the nucleation suppressing effect of small nanostructures. The coverage of the fluorosilane coating should be examined and improved. The nanostructure and thickness of the coating should be investigated, to determine how it interacts with the nanoroughness provided by the silica particles.

Additionally, environmental factors such as the condensation of humidity was suspected to have a large influence on the anti-icing properties. Simulating real environmental conditions during testing should be prioritized going forward. The behaviour of the coating under such conditions needs to be examined. The influence of surface structuring on humidity and frost formation should be investigated. Less emphasis should be put on maximising hydrophobicity through surface structuring, as it was not found to be correlated with anti-icing properties. The coating durability should be considered, and especially how it is affected by icing.

The ability of a surface to remove supercooled, impacting droplets is another potential anti-icing behaviour of hydrophobic surfaces, but it was not examined in this work. The surface ice adhesion and mechanical properties would be important for industrial applications, and would thus be essential to optimize.

Bibliography

[1] Hanna Sandvoll Vassmyr. Development of hydrophobic surfaces for anti-icing applications. Master's thesis, NTNU, 2016.

[2] Raymond Luneng. Development of hydrophobic surfaces for anti-icing applications. Master's thesis, NTNU, 2015.

[3] Ole-Bjørn Ellingsen Moe. Development of hydrophobic surfaces for anti-icing applications. Master's thesis, NTNU, 2015.

[4] C. Antonini, M. Innocenti, T. Horn, M. Marengo, and A. Amirfazli. Understanding the effect of superhydrophobic coatings on energy reduction in anti-icing systems. *Cold Regions Science and Technology*, 67(1 - 2):58 – 67, 2011.

[5] Richard Menini and Masoud Farzaneh. Advanced icephobic coatings. *Journal of Adhesion Science and Technology*, 25(9):971–992, 2011.

[6] Masoud Farzaneh. *Atmospheric icing of power networks*. Springer Science & Business Media, 2008.

[7] Friedrich Kiessling, Peter Nefzger, Joao Felix Nolasco, and Ulf Kaintzyk. *Overhead power lines: planning, design, construction*. Springer, 2014.

[8] Bjørn Egil Kringlebotn Nygaard, Hálfdán Ágústsson, and Katalin Somfalvi-Tóth. Modeling wet snow accretion on power lines: improvements to previous methods using 50 years of observations. *Journal of Applied Meteorology and Climatology*, 52(10):2189–2203, 2013.

[9] Matthew Carl Homola. *Atmospheric icing on wind turbines*. PhD thesis, Norwegian University of Science and Technology, September 2011.

[10] Stefan Jung, Marko Dorrestijn, Dominik Raps, Arindam Das, Constantine M Megaridis, and Dimos Poulikakos. Are superhydrophobic surfaces best for icephobicity? *Langmuir*, 27(6):3059–3066, 2011.

[11] Stewart G Cober, George A Isaac, and J Walter Strapp. Characterizations of aircraft icing environments that include supercooled large drops. *Journal of Applied Meteorology*, 40(11):1984–2002, 2001.

[12] Michael J Kreder, Jack Alvarenga, Philseok Kim, and Joanna Aizenberg. Design of anti-icing surfaces: smooth, textured or slippery? *Nature Reviews Materials*, 1:15003, 2016.

[13] Øyvind Lie. Sjekk hvordan statnetts toppliner ises ned om vinteren. *Teknisk Ukeblad*, 29 August 2014. Available at `http://www.tu.no/kraft/2014/08/29/sjekk-hvordan-statnetts-toppliner-ises-ned-om-vinteren`. News article online. Accessed [2017-06-28].

[14] Jannicke Nilsen. Her spyler helikopteret bort et tykt lag med is. *Teknisk Ukeblad*, 01 February 2015. Available at `https://www.tu.no/artikler/her-spyler-helikopteret-bort-et-tykt-lag-med-is/222975`. News article online. Accessed [2017-06-28].

[15] JL Laforte, MA Allaire, and J Laflamme. State-of-the-art on power line de-icing. *Atmospheric Research*, 46(1):143–158, 1998.

[16] Masoud Farzaneh, Christophe Volat, and André Leblond. Anti-icing and de-icing techniques for overhead lines. In Masoud Farzaneh, editor, *Atmospheric Icing of Power Networks*, chapter 6, pages 229–268. Springer Science+Business Media B.V., 2008.

[17] Olivier Parent and Adrian Ilinca. Anti-icing and de-icing techniques for wind turbines: Critical review. *Cold regions science and technology*, 65(1):88–96, 2011.

[18] Devikarani M Ramakrishna and Thiruvenkatachari Viraraghavan. Environmental impact of chemical deicers–a review. *Water, Air, and Soil Pollution*, 166(1-4):49–63, 2005.

[19] Wilhelm Barthlott and Christoph Neinhuis. Purity of the sacred lotus, or escape from contamination in biological surfaces. *Planta*, 202(1):1–8, 1997.

[20] Lin Feng, Shuhong Li, Yingshun Li, Huanjun Li, Lingjuan Zhang, Jin Zhai, Yanlin Song, Biqian Liu, Lei Jiang, and Daoben Zhu. Super-hydrophobic surfaces: from natural to artificial. *Advanced materials*, 14(24):1857–1860, 2002.

[21] Thomas M Schutzius, Stefan Jung, Tanmoy Maitra, Patric Eberle, Carlo Antonini, Christos Stamatopoulos, and Dimos Poulikakos. Physics of icing and rational design of surfaces with extraordinary icephobicity. *Langmuir*, 2014.

[22] Ludmila Boinovich, Alexandre M Emelyanenko, Vadim V Korolev, and Andrei S Pashinin. Effect of wettability on sessile drop freezing: When superhydrophobicity stimulates an extreme freezing delay. *Langmuir*, 30(6):1659–1668, 2014.

[23] Adam J Meuler, J David Smith, Kripa K Varanasi, Joseph M Mabry, Gareth H McKinley, and Robert E Cohen. Relationships between water wettability and ice adhesion. *ACS applied materials & interfaces*, 2(11):3100–3110, 2010.

[24] SA Kulinich and M Farzaneh. How wetting hysteresis influences ice adhesion strength on superhydrophobic surfaces. *Langmuir*, 25(16):8854–8856, 2009.

[25] Qitao Fu, Xinghua Wu, Divya Kumar, Jeffrey WC Ho, Pushkar D Kanhere, Narasimalu Srikanth, Erjia Liu, Peter Wilson, and Zhong Chen. Development of sol–gel icephobic coatings: effect of surface roughness and surface energy. *ACS applied materials & interfaces*, 6(23):20685–20692, 2014.

[26] Aase Marie Halvorsen. Hydrophobic coatings for anti-icing applications. Master's thesis, NTNU, 2014.

[27] Ellen-Kristin Raasok. Hydrophobic coatings for anti-icing applications. Master's thesis, NTNU, 2014.

[28] Paul C Hiemenz and Raj Rajagopalan. *Principles of colloid and surface chemistry*. CRC press, 1997.

[29] NB Vargaftik, BN Volkov, and LD Voljak. International tables of the surface tension of water. *Journal of Physical and Chemical Reference Data*, 12(3):817–820, 1983.

[30] Pierre-Gilles De Gennes, Françoise Brochard-Wyart, and David Quéré. *Capillarity and wetting phenomena: drops, bubbles, pearls, waves*. Springer Science & Business Media, 2004.

[31] Takashi Nishino, Masashi Meguro, Katsuhiko Nakamae, Motonori Matsushita, and Yasukiyo Ueda. The lowest surface free energy based on- cf3 alignment. *Langmuir*, 15(13):4321–4323, 1999.

[32] Golrokh Heydari, Esben Thormann, Mikael Järn, Eric Tyrode, and Per M Claesson. Hydrophobic surfaces: topography effects on wetting by supercooled water and freezing delay. *The Journal of Physical Chemistry C*, 117(42):21752–21762, 2013.

[33] Sigma-Aldrich. Sigma-aldrich product catalogue. `http://www.sigmaaldrich.com/catalog/product/aldrich/667420?lang=en&region=NO`. Accessed [2017-04-13].

[34] D Gupta and ML Gulrajani. Self cleaning finishes for textiles. *Functional Finishes for Textiles: Improving Comfort, Performance and Protection*, page 257, 2014.

[35] Zonglin Chu and Stefan Seeger. Superamphiphobic surfaces. *Chemical Society Reviews*, 43(8):2784–2798, 2014.

[36] Thomas Young. An essay on the cohesion of fluids. *Philosophical Transactions of the Royal Society of London*, 95:65–87, 1805.

[37] David Quéré. Wetting and roughness. *Annu. Rev. Mater. Res.*, 38:71–99, 2008.

[38] David Quéré. Non-sticking drops. *Reports on Progress in Physics*, 68(11):2495, 2005.

[39] Aurélie Lafuma and David Quéré. Superhydrophobic states. *Nature materials*, 2(7):457–460, 2003.

[40] Handong Cho, Dongseob Kim, Changwoo Lee, and Woonbong Hwang. A simple fabrication method for mechanically robust superhydrophobic surface by hierarchical aluminum hydroxide structures. *Current Applied Physics*, 13(4):762–767, 2013.

[41] Xianming Shi, Tuan Anh Nguyen, Zhiyong Suo, Jianlin Wu, Jing Gong, and Recep Avci. Electrochemical and mechanical properties of superhydrophobic aluminum substrates modified with nano-silica and fluorosilane. *Surface and Coatings Technology*, 206(17):3700–3713, 2012.

[42] Robert N Wenzel. Resistance of solid surfaces to wetting by water. *Industrial & Engineering Chemistry*, 28(8):988–994, 1936.

[43] ABD Cassie and S Baxter. Wettability of porous surfaces. *Transactions of the Faraday Society*, 40:546–551, 1944.

[44] M Reyssat, JM Yeomans, and D Quéré. Impalement of fakir drops. *EPL (Europhysics Letters)*, 81(2):26006, 2007.

[45] Hans-Jürgen Butt, Karlheinz Graf, and Michael Kappl. *Physics and Chemistry of Interfaces. Third, Revised and Enlarged Edition.* WILEY-VCH Verlag GmbH & Co. KGaA, 2013.

[46] H. B. Eral, D. J. C. M. 't Mannetje, and J. M. Oh. Contact angle hysteresis: a review of fundamentals and applications. *Colloid and Polymer Science*, 291(2):247–260, 2013.

[47] Bharat Bhushan and Michael Nosonovsky. The rose petal effect and the modes of superhydrophobicity. *Philosophical Transactions of the Royal Society A: Mathematical, Physical and Engineering Sciences*, 368(1929):4713–4728, 2010.

[48] Xi Zhang, Feng Shi, Jia Niu, Yugui Jiang, and Zhiqiang Wang. Superhydrophobic surfaces: from structural control to functional application. *Journal of Materials Chemistry*, 18(6):621–633, 2008.

[49] Minglin Ma and Randal M Hill. Superhydrophobic surfaces. *Current opinion in colloid & interface science*, 11(4):193–202, 2006.

[50] KS Birdi, DT Vu, and A Winter. A study of the evaporation rates of small water drops placed on a solid surface. *The Journal of physical chemistry*, 93(9):3702–3703, 1989.

[51] C Bourges-Monnier and MER Shanahan. Influence of evaporation on contact angle. *Langmuir*, 11(7):2820–2829, 1995.

[52] SA Kulinich and M Farzaneh. Effect of contact angle hysteresis on water droplet evaporation from super-hydrophobic surfaces. *Applied Surface Science*, 255(7):4056–4060, 2009.

[53] Piotr Tourkine, Marie Le Merrer, and David Quéré. Delayed freezing on water repellent materials. *Langmuir*, 25(13):7214–7216, 2009.

[54] SA Kulinich and M Farzaneh. Ice adhesion on super-hydrophobic surfaces. *Applied Surface Science*, 255(18):8153–8157, 2009.

[55] Liangliang Cao, Andrew K Jones, Vinod K Sikka, Jianzhong Wu, and Di Gao. Anti-icing superhydrophobic coatings. *Langmuir*, 25(21):12444–12448, 2009.

[56] Fochi Wang, Chengrong Li, Yuzhen Lv, Fangcheng Lv, and Yuefan Du. Ice accretion on superhydrophobic aluminum surfaces under low-temperature conditions. *Cold regions science and technology*, 62(1):29–33, 2010.

[57] SA Kulinich, S Farhadi, K Nose, and XW Du. Superhydrophobic surfaces: are they really ice-repellent? *Langmuir*, 27(1):25–29, 2010.

[58] Vahid Hejazi, Konstantin Sobolev, and Michael Nosonovsky. From superhydrophobicity to icephobicity: forces and interaction analysis. *Scientific reports*, 3, 2013.

[59] Patric Eberle, Manish K Tiwari, Tanmoy Maitra, and Dimos Poulikakos. Rational nanostructuring of surfaces for extraordinary icephobicity. *Nanoscale*, 6(9):4874–4881, 2014.

[60] Stefan Jung, Manish K Tiwari, N Vuong Doan, and Dimos Poulikakos. Mechanism of supercooled droplet freezing on surfaces. *Nature communications*, 3:615, 2012.

[61] Linda Oberli, Dean Caruso, Colin Hall, Manrico Fabretto, Peter J Murphy, and Drew Evans. Condensation and freezing of droplets on superhydrophobic surfaces. *Advances in colloid and interface science*, 210:47–57, 2014.

[62] WM Ketcham and PV Hobbs. An experimental determination of the surface energies of ice. *Philosophical Magazine*, 19(162):1161–1173, 1969.

[63] Vaibhav Bahadur, Lidiya Mishchenko, Benjamin Hatton, J Ashley Taylor, Joanna Aizenberg, and Tom Krupenkin. Predictive model for ice formation on superhydrophobic surfaces. *Langmuir*, 27(23):14143–14150, 2011.

[64] Golrokh Heydari, Maziar Sedighi Moghaddam, Mikko Tuominen, Matthew Fielden, Janne Haapanen, Jyrki M Mäkelä, and Per M Claesson. Wetting hysteresis induced by temperature changes: Supercooled water on hydrophobic surfaces. *Journal of colloid and interface science*, 468:21–33, 2016.

[65] Rosaria Ciriminna, Alexandra Fidalgo, Valerica Pandarus, François Béland, Laura M Ilharco, and Mario Pagliaro. The sol–gel route to advanced silica-based materials and recent applications. *Chemical reviews*, 113(8):6592–6620, 2013.

[66] Larry L. Hench and Jon K. West. The sol-gel process. *Chemical Reviews*, 90(1):33–72, 1990.

[67] Sidsel Meli Hanetho. *Hybrid Aminopropyl Silane-based Coatings on Steel*. PhD thesis, Norwegian University of Science and Technology, October 2012.

[68] C Jeffrey Brinker and George W Scherer. *Sol-Gel Science: The Physics and Chemistry of Sol-Gel Processing*. Academic Press Inc., 1990.

[69] C Jeffrey Brinker and Alan J Hurd. Fundamentals of sol-gel dip-coating. *Journal de Physique III*, 4(7):1231–1242, 1994.

[70] Sigma-Aldrich. Sigma-aldrich product catalogue. `http://www.sigmaaldrich.com/catalog/product/aldrich/333859?lang=en&region=NO`. Accessed [2017-04-13].

[71] Brian L Cushing, Vladimir L Kolesnichenko, and Charles J O'Connor. Recent advances in the liquid-phase syntheses of inorganic nanoparticles. *Chemical reviews*, 104(9):3893–3946, 2004.

[72] Werner Stöber, Arthur Fink, and Ernst Bohn. Controlled growth of monodisperse silica spheres in the micron size range. *Journal of Colloid and Interface Science*, 26(1):62 – 69, 1968.

[73] DL Green, JS Lin, Yui-Fai Lam, MZ-C Hu, Dale W Schaefer, and MT Harris. Size, volume fraction, and nucleation of stober silica nanoparticles. *Journal of colloid and interface science*, 266(2):346–358, 2003.

[74] VM Masalov, NS Sukhinina, EA Kudrenko, and GA Emelchenko. Mechanism of formation and nanostructure of stöber silica particles. *Nanotechnology*, 22(27):275718, 2011.

[75] Victor K. LaMer and Robert H. Dinegar. Theory, production and mechanism of formation of monodispersed hydrosols. *Journal of the American Chemical Society*, 72(11):4847–4854, 1950.

[76] GH Bogush and CF Zukoski. Studies of the kinetics of the precipitation of uniform silica particles through the hydrolysis and condensation of silicon alkoxides. *Journal of Colloid and Interface Science*, 142(1):1–18, 1991.

[77] Satish A Mahadik, DB Mahadik, MS Kavale, VG Parale, PB Wagh, Harish C Barshilia, Satish C Gupta, ND Hegde, and A Venkateswara Rao. Thermally stable and transparent superhydrophobic sol–gel coatings by spray method. *Journal of sol-gel science and technology*, 63(3):580–586, 2012.

[78] Jian Li, Yushun Zhao, Jianlin Hu, Lichun Shu, and Xianming Shi. Anti-icing performance of a superhydrophobic pdms/modified nano-silica hybrid coating for insulators. *Journal of Adhesion Science and Technology*, 26(4-5):665–679, 2012.

[79] Qianqian Shang, Yonghong Zhou, and Guomin Xiao. A simple method for the fabrication of silica-based superhydrophobic surfaces. *Journal of Coatings Technology and Research*, 11(4):509–515, 2014.

[80] Joseph R Davis et al. *Aluminum and aluminum alloys*. ASM international, 1993.

[81] Euro Inox. Stainless steel: tables of technical properties. *Material and application series*, page 5, 2007.

[82] T Yasuda, T Okuno, and H Yasuda. Contact angle of water on polymer surfaces. *Langmuir*, 10(7):2435–2439, 1994.

[83] Charles W Extrand. Model for contact angles and hysteresis on rough and ultraphobic surfaces. *Langmuir*, 18(21):7991–7999, 2002.

[84] Lichao Gao and Thomas J McCarthy. How wenzel and cassie were wrong. *Langmuir*, 23(7):3762–3765, 2007.

[85] Lichao Gao and Thomas J McCarthy. An attempt to correct the faulty intuition perpetuated by the wenzel and cassie "laws". *Langmuir*, 25(13):7249–7255, 2009.

[86] H Yildirim Erbil and C Elif Cansoy. Range of applicability of the wenzel and cassie- baxter equations for superhydrophobic surfaces. *Langmuir*, 25(24):14135–14145, 2009.

[87] Wonjae Choi, Anish Tuteja, Joseph M Mabry, Robert E Cohen, and Gareth H McKinley. A modified cassie–baxter relationship to explain contact angle hysteresis and anisotropy on non-wetting textured surfaces. *Journal of colloid and interface science*, 339(1):208–216, 2009.

[88] Hua Hu and Ronald G Larson. Evaporation of a sessile droplet on a substrate. *The Journal of Physical Chemistry B*, 106(6):1334–1344, 2002.

[89] Zhongliang Liu, Yunjun Gou, Jieteng Wang, and Shuiyuan Cheng. Frost formation on a super-hydrophobic surface under natural convection conditions. *International Journal of Heat and Mass Transfer*, 51(25):5975–5982, 2008.

[90] Ludmila B Boinovich, Alexandre M Emelyanenko, Vladimir K Ivanov, and Andrei S Pashinin. Durable icephobic coating for stainless steel. *ACS applied materials & interfaces*, 5(7):2549–2554, 2013.